UNIVERSITY of CALIFORNIA
SANTA CRUZ

THE EVOLUTION OF SUPERNOVAE EMBEDDED IN STELLAR GROUPS

A thesis submitted in partial satisfaction of the
requirements for the degree of

BACHELOR OF SCIENCE

in

PHYSICS

by

Matthew S. B. Coleman

9 June 2011

The thesis of Matthew S. B. Coleman is approved by:

Professor Enrico Ramirez-Ruiz Advisor	Professor Adriane Steinacker Theses Coordinator

Professor David P. Belanger
Chair, Department of Physics

Abstract

The Evolution of Supernovae Embedded in Stellar Groups

by

Matthew S. B. Coleman

Supernovae (SNe) and the remnants they leave behind dramatically impact the dynamics of the interstellar medium. They are also likely the source of all but the highest energy cosmic rays, and they are the means by which heavy elements are produced and disseminated. The standard model used for the evolution of supernova remnants (SNRs) has been based on Woltjer's (1972) simplistic model describing SNRs as spherical shells in one of four distinct phases of expansion into uniform media. These phases have come to be known as *free expansion*, *Sedov, adiabatic blast wave*, *radiative snowplow*, and *dispersal*. Yet the evidence is strong that this cartoon is inadequate as a model for real SNR dynamics. The distinct phases imagined by Woltjer may be brief or may not occur at all in a given remnant. Further, SNRs are generally not spherical and do not interact with uniform media. Thus, different dynamical stages may occur simultaneously within a single remnant, and structures may be very complex. The observational and theoretical evidence of this dynamical complexity seriously limits our ability to determine critical issues ranging from SNR age determination to their role in establishing the structure of the ISM. This thesis was conceived to address key questions regarding the evolution of supernovae embedded in the complex environments found in and around young stellar groups by means of three dimensional, hydrodynamical calculations. Because massive star progenitors in groups are expected to have their close-in surroundings modified by the winds of their neighboring stars,

we consider shocked winds as possible external media for supernova remnant evolution. Abundant confirmation is provided here of the important notion that the morphology and visibility of supernova remnants are determined largely by their circumstellar environments.

Contents

List of Figures

List of Tables

To

my fiancée Rae, and to my mother Jackie. Without their love and support I would not be as successful as I am today, nor would this thesis exist.

Acknowledgements

I want to thank my advisors, Enrico and Rachel. Their consistent insight and help made this thesis possible.

1

Introduction

Supernovae (SNe) are some of the most violent and luminous events in the universe capable of briefly outshining an entire galaxy. These energetic events enrich their surroundings with metals, and are therefore indirectly responsible for our existence. This is only one of the many reasons why supernovae are of great interest to astronomers. In this thesis, I will explore how SNe interact with the complex and dynamic environments from which they were born. I will start with developing the background needed to understand SN environments and motivate the topic of my thesis.

1.1 Massive Stellar Evolution

To understand SNe, it is necessary to understand the massive stars that create these explosive events when they exhaust their fuel. In this thesis I define a "massive star" as a star with a main sequence mass exceeding about ten solar masses ($M > 10M_{\odot}$), thought to end its life as a supernova leaving its core behind as a neutron star.

Massive stars burn brighter and perish more dramatically than most other stars.

Massive stars require higher central temperatures to balance the greater pull of gravity. Thus massive stars produce helium from hydrogen through the CNO cycle rather than the P-P Chain. These higher central temperatures and pressure also prevent the stellar core from becoming electron degenerate at the onset of helium burning, thus there is no helium flash. When a star ten times more massive then Sun exhaust the helium in the core, the nuclear fusion cycle continues. The carbon core contracts further and reaches high enough temperature to burn carbon to oxygen, neon, silicon, sulphur and finally to iron (See Figure 1.1).

Iron is the most stable form of nuclear matter and there is no energy to be gained by converting it to any heavier element. Without a source of heat to counteract gravity, the iron core collapses until it reaches nuclear densities. This high density core resists further collapse essentially creating a surface for the in-falling matter to 'bounce' off. This sudden core bounce (which includes the release of energetic neutrinos from the core) produces a supernova explosion, allowing the star to outshine a galaxy for an entire month. Supernova explosions inject carbon, oxygen, silicon and other heavy elements up to, and even surpassing iron into interstellar space, and are the source of heavy elements in the universe.

1.1.1 Compact Object Formation

The collapse of these massive stellar cores results in the formation of one of two types of compact objects: black holes and neutron stars. The beginning stages of formation of these two types of objects are virtually the same. As nuclear burning progresses in an old massive star, reactants become depleted and iron accumulates in the core. As fuel runs out, so does the pressure supporting the star, causing it to contract and heat the core, creating

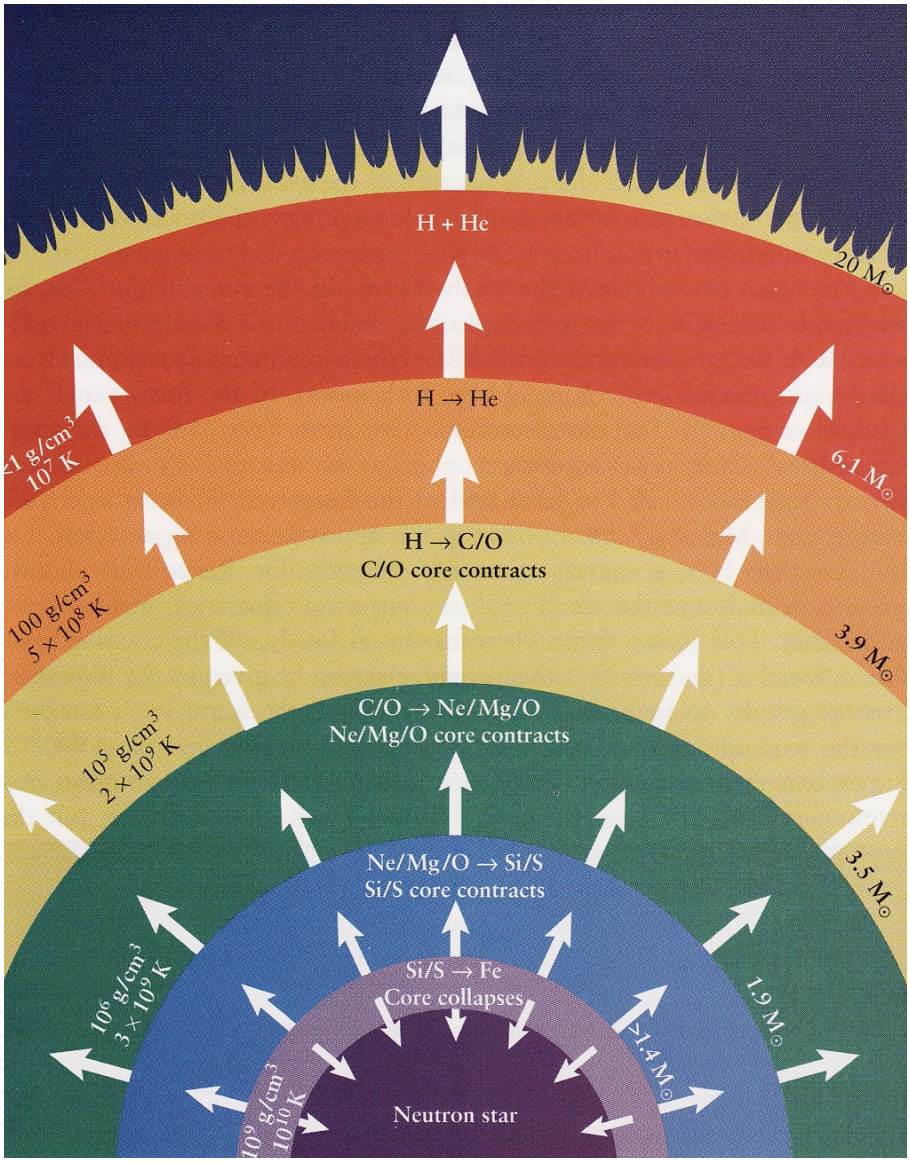

Figure 1.1 Shell burning diagram (Taken from Begelman & Rees 2010). This figure shows the stratification of elements (with lighter elements toward the exterior) and nuclear burning that occurs at late stages in a massive star's life.

an environment where photons posses enough energy to rip apart atoms in a process called photodisintegration. The particularly important photodisintegration reactions are

$$^{56}_{26}\mathrm{Fe} + \gamma \rightarrow 13\,^{4}_{2}\mathrm{He} + 4n \tag{1.1}$$

$$^{4}_{2}\mathrm{He} + \gamma \rightarrow 2p^{+} + 2e^{-} + 2n, \tag{1.2}$$

with electron capturing occurring simultaneously:

$$p^{+} + e^{-} \rightarrow n + \nu_{e}. \tag{1.3}$$

These destructive reactions cause the core to collapse. The collapsing core at this stage is primarily neutrons, which, like all fermions, obey the Pauli exclusion principle. This forbids neutrons from sharing the same energy state, resulting in an additional pressure (degeneracy pressure) when neutrons are forced into similar quantum states by compressive forces such as gravity. At this point there are two possibilities, which correspond to whether gravity is stronger or weaker than the neutron degeneracy pressure (See Figure 1.2). Various parameters define the ultimate fate of a massive star, primarily its mass. Stars more massive than $\sim 25M_{\odot}$are thought to have gravitational fields too strong for any known support mechanism, and ultimately collapse into a singularity known as a black hole (See Figure 1.2). It is unclear if this complete collapse can result in the energetic explosion associated with a typical supernova although recent theroetical work suggests black hole formation might be responsible for hypernova explosions.

Stars less massive than about $\sim 25M_{\odot}$ are fortunate; they are able to overcome their own gravitational field by utilizing neutron degeneracy pressure. By relying on this

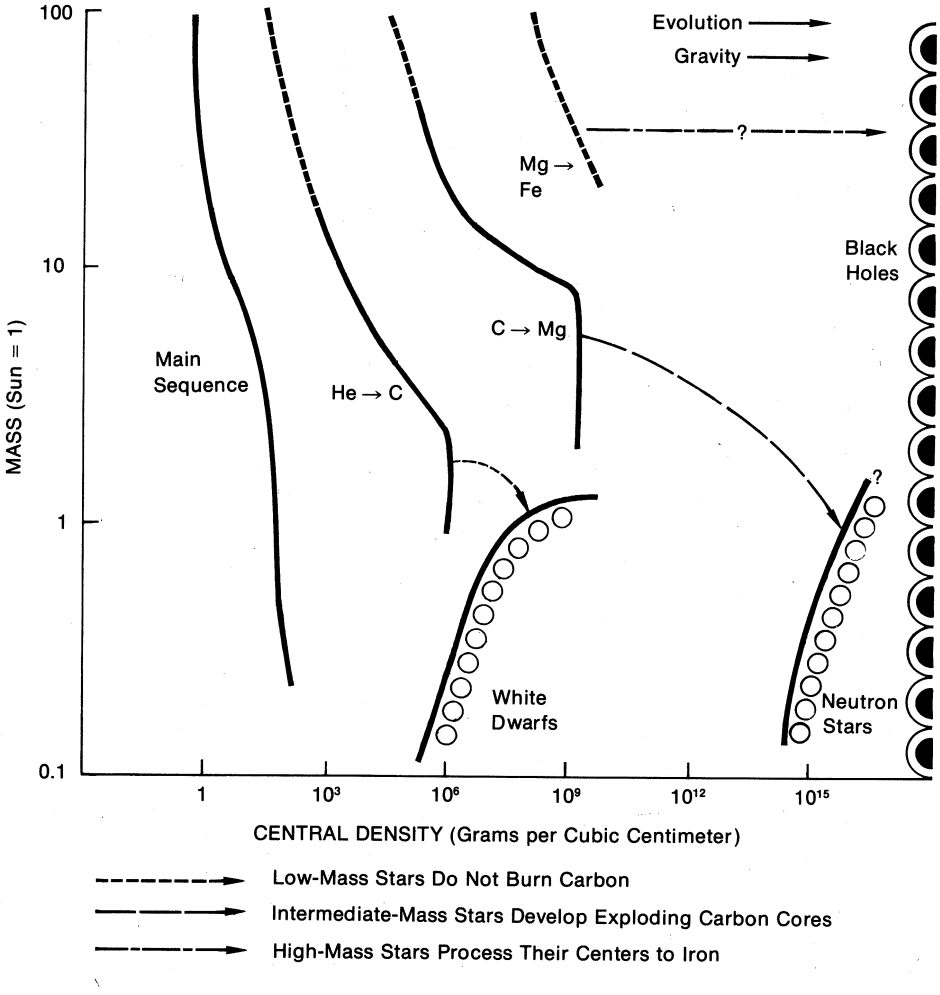

Figure 1.2 Stellar fate diagram. Each vertical curve represents the whole spectrum of stars at different states in stellar evolution, with the farthest most right curve corresponding to the main sequence. The other curves are labeled with the fusion reactions that are occurring. The vertical axis corresponds to the mass of a star and the horizontal axis corresponds to the central density. Lower mass stars can not make it pass the He burning state and end up as white dwarfs. The midrange of stars (those considered in this thesis) end up as neutron stars. Finally, the extremely massive stars end their lives as black holes.

last crutch, a stellar core is forced into a ball of mostly neutrons i.e a neutron star. The outer layers of the star fall inward and reflect off the "surface" of the newly formed neutron star. Essentially degeneracy pressure is flipped on like a switch, thus acting like a hard surface for infalling matter to be reflected, resulting in the development of a bounce. This flow has velocities much greater than sound speed in the environment around the neutron star and thus form a shock wave, whose outward momentum is then subsequently increase by neutrino interactions.

1.1.2 Supernovae

This outward shock is what defines the spectacular stellar explosions known as core collapse supernovae (CCSNe). The reflected infalling matter that created this shock wave is not, however, the main source of energy for a SN; gravitational binding energy released from the creation of a neutron star is responsible for producing the intense energies displayed by SNe. To see this, first consider the gravitational binding energy (E_{grav}) of a neutron star in terms of typical parameters:

$$E_{\text{grav}} \approx \frac{GM_{NS}^2}{R_{NS}} \approx 3 \times 10^{53} \text{ ergs } \times \left(\frac{M_{NS}}{1.4M_{\odot}}\right)^2 \left(\frac{R_{NS}}{15 \text{ km}}\right)^{-1} \tag{1.4}$$

where M_{NS} is the mass of the neutron star and R_{NS} is its radius. This energy is radiated by neutrinos from nuclear processes such as electron capture (1.3). Despite the weakly interacting nature of neutrinos, the shock created by the reflected infalling stellar matter is dense enough to couple with $\sim 1\%$ of the neutrinos, transferring $\sim 10^{51}$ ergs of neutrino energy to the outward shock and ejecta. Up until February of 1987, it was not known if this description of neutrino emission and coupling to matter in the shock was accurate. Then

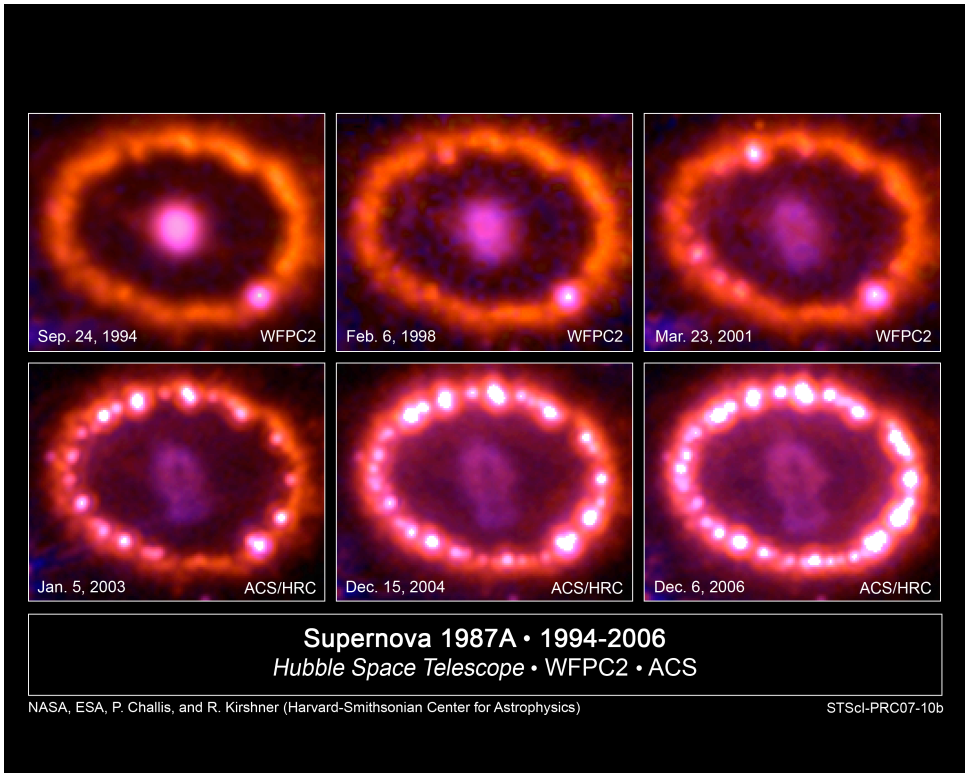

Figure 1.3 Remnant of supernova 1987A. Hubble Space Telescope composite optical observations of SNR 1987A overtime.

the first extrasolar neutrinos were detected, three hours before light from the same event arrived, marking the discovery of supernova 1987A (SN1987A). By analyzing the detected neutrinos, it was determined that neutrinos emitted by SN1987A radiated $2 - 3 \times 10^{53}$ ergs away, marking the creation of a $1.40 \pm 0.15 M_{\odot}$ mass neutron star (Woosley 1988). Despite repeated imaging of the supernova remnant in multiple wavelengths (see Figure 1.3) there has, unfortunately, been no direct detections of a stellar remnant. These images give us detailed information on how SN1987A continues to evolve as a supernova remnant (SNR). SNR are the continually evolving "leftovers" from a supernova that were not integrated into the neutron star. The kinetic energy of the supernova ($\sim 10^{51}$ ergs) goes into expanding the shock wave and heating the interstellar medium (ISM). Initially the resistance exerted by ISM on a SNR is negligible, allowing the adiabatic free expansion of the SNR. As an SNR expands, the swept-up mass approaches the mass of the ejecta, at which point the shock wave no longer undergoes free expansion and decelerates. This deceleration creates a reverse shock is generated, i.e. a shock that moves inward relative to the ejecta (e.g., McKee 1974). The kinetic energy from this inward shock is converted into thermal energy, heating the ejecta to several million degrees, causing the SNR to bright in the X-rays. Additionally, the reverse shock increases pressure in the interior of the SNR and by the time the reverse finishes propagating inward the swept up mass is significantly larger then the initial mass of the SNR, causing the progression of the outward shock wave to follow the Sedov-Taylor solution (Sedov 1946; Taylor 1950; Sedov 1959). This solution used dimensional arguments to relate the radius of the expanding shock (R_s) to the energy of the supernova ($E_{\rm SN}$), the ambient density (ρ_0) and the time elapsed since the explosion (t). The Sedov-Taylor

solution is as follows:

$$R_s = 5.91 \text{ pc } \times \left(\frac{E_{\rm SN}}{10^{51} \text{ ergs}}\right)^{1/5} \left(\frac{\rho_0}{10^{-24} \text{ g cm}^{-3}}\right)^{-1/5} \left(\frac{t}{1000 \text{ yr}}\right)^{2/5}. \quad (1.5)$$

the Sedov-Taylor solution is further discussed in Chapter 3. As the SNR continues to expand and cool, line emission becomes efficient and the SNR is observable for roughly $\sim$ 20 kyr (Braun et al. 1989). Finally, after roughly $\sim 10^6$ years the expansion of a SNR has slowed to speeds comparable to the velocity dispersion of the ISM. Thus allowing the SNR to become fully dispersed into the ISM.

1.2 The Stellar Afterlife: Neuron Stars

After a SNR is dispersed into the ISM, its massive progenitor will continue to exist as a neutron star. Neutron stars come in a few flavors, with most categories being sub-classes of pulsars. All pulsars are fast rotators with powerful magnetic fields whose magnetic poles do not line up with the axis of rotation (See Figure 1.4). These magnetic fields direct inflowing gas to along the magnetic field lines, impacting the neutron star in its magnetic polar regions. Thus producing a beam of photons along the magnetic poles. As a neutron star rotates so do its magnetic pole, creating a lighthouse effect with a steady period making pulsars readily observable. So far, three main types of pulsars have been observed, each corresponding to different energy sources: rotation-powered pulsars, which are powered by the loss of rotational energy and tend to emit radio signals; accretion-powered pulsars, which generate x-rays by accreting mater from a binary companion; and magnetars. Magnetars are young neutron stars with strong magnetic fields $> 10^{14}$ G.

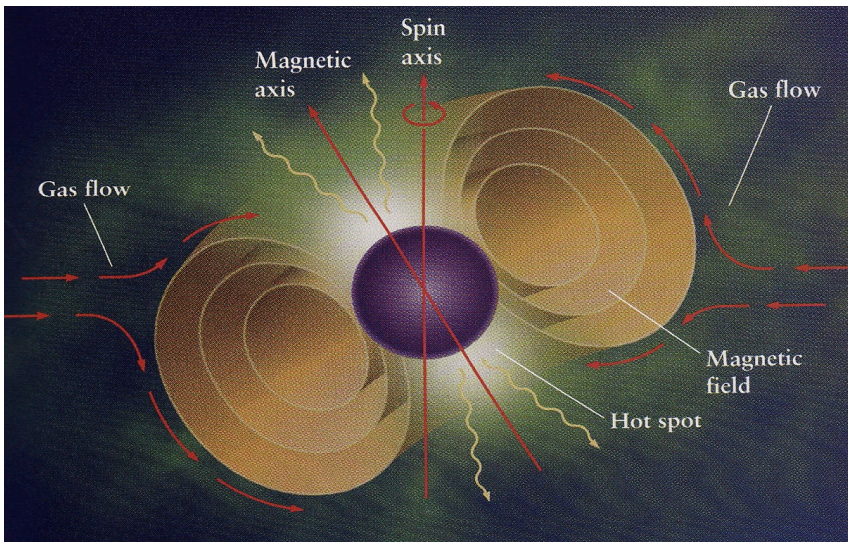

Figure 1.4 Accretion powered pulsar diagram. This diagram shows the pulsar in purple with th cross section of its magnetic fields in orange (Taken from Begelman & Rees 2010). Also shown are the rotation axis and magnetic pole, which are offset from each other. For accretion powered pulsars, gas flows in around the magnetic fields and onto the surface of the neutron star, generating radiation which is released along the magnetic pole marked at the "hot spot" in the diagram (other types of pulsars also radiate along the magnetic pole). As the pulsar rotates so does its magnetic pole, crating a lighthouse effect that gives pulsars their name.

Two classes of observed phenomena are believed to be caused by magnetars: Soft Gamma Repeaters (SGRs) and Anomalous X-ray Pulsars (AXPs). SGRs were originally discovered as brief bursts of gamma rays, and many of these bursts were later associated with an X-ray pulsar (Woods & Thompson 2006). AXP are X-ray pulsars with persistent pulses, but some have exhibited SGR-like bursts (Woods & Thompson 2006). Despite requiring different methods of detection, these two types of neutron stars have extremely energetic pulses or bursts that are inconsistent with accretion-powered pulsars, thus they are thought to be the same kind of object, i.e. a magnetar. Most magnetars with observationally determined ages have spin down ages $\lesssim 5 \times 10^3$ years (Woods & Thompson 2006). Their spin down age, determined by the rate at which a magnetar loses angular momentum due to dipole radiation effects ($\tau = P/2\dot{P}$) is commonly assumed to be similar to the magnetar's age. Owing to their intense magnetic fields, magnetars radiate energy away relatively quickly through dipole radiation and quantum effects, and thus have estimated lifetimes on the order of only 10^4 years. Unfortunately, due to our lack of knowledge of the structure of magnetic fields around magnetars, it is not clear how accurate these estimates are. Despite this uncertainty in magnetar ages, these objects are likely significantly younger than the observability timescale for SNR ($\sim$ 20 kyr, Braun et al. 1989), leading one to believe, that in most cases, the environments magnetars reside in should show some sign of the SNR that was created by the stellar collapse. To date, however, only seven of the 21 magnetars (16 confirmed and five candidates) have SNR associations[1]. To find an answer to this dilemma we must gain a better understanding of the environments that massive stars, and therefore magnetars, live in.

[1]for an updated catalog of magnetars, see `http://www.physics.mcgill.ca/~pulsar/magnetar/main.html`

1.3 The Stellar Neighborhood

Massive stars are primarily found in environments where nearby stars are plentiful and are rarely found in isolation (Hillenbrand 1997). It is believed that forming massive stars in isolation is extremely unlikely because as gas attempts to accrete into a star more massive than $\sim 10 M_{\odot}$ significant energy is radiated. The radiation pressure generated halts the accretion process and thus additional an gravitational potential is thought to be needed (Bonnell et al. 1998). This gravitational potential comes from the formation of neighboring stars which bring in additional mass increasing the entire gravitation potential of the proto-group, allowing even more mass to be accreted. Stellar neighborhoods come in a variety of sizes and densities, like neighborhoods here on Earth do. On the rural side of the spectrum are OB associations which contain ~ 10 massive stars (classified as O or B type stars) within a few cubic parsecs. The relatively low density of these associations leaves them gravitationally unbound. Open clusters are the suburbia of stellar neighborhoods, containing a few hundred stars in a volume that is ~ 10 pc across and are loosely bound by gravity. Massive stars are centrally concentrated in in most groups. Finally a metropolitan area is analogous to globular clusters, which contain between $\sim 10^4$ and $\sim 10^6$ stars in about the same volume as open clusters, and are therefore strongly gravitationally bound. For the purposes of this thesis, it does not matter whether these stellar neighborhoods are gravitationally bound. Therefore, I refer to the three stellar neighborhoods mentioned above (and the spectrum in between) as stellar groups. Additionally, I am only concerned with the massive stars in these groups for two reasons: they will produce SN, and the stellar winds of less massive stars are negligible compared to massive stellar winds. The winds from massive stars are what makes stellar groups such complex and dynamic environments.

1.4 Supernovae in Stellar Groups

Prior to this work, only a few types of interactions between SNRs and stellar winds have been studied. Some work has been done on SNR interactions with our own solar system (Fields et al. 2008; Athanassiadou 2009), and with the wind of the progenitor star (Marsden et al. 2001; Pan et al. 2010). Others have also examined how supernovae can affect clusters through the mechanisms of gas expulsion (Decressin et al. 2010) and enrichment and heating (Bailin & Harris 2009). However, with the exception of this work, there has only been one attempt to model SN interacting with multiple stellar winds (Rockefeller et al. 2005), which simulates a SN exploding in the center of the galaxy, instead of the stellar group environments considered here. In this thesis I seek to understand how SNe interact with their progenitor stellar groups. The stellar winds in these groups are constantly interacting with each other and create standing shocks. It is not clear from first principles, how these winds and standing shocks interact with a SN, and alter its evolution. This is a complex hydrodynamical problem which is inherently impossible to solve analytically. Therefore, I deploy the use of computational hydrodynamics to seek out an accurate description of the problem. The structure of this thesis is as follows. Chapter 2 lays out the computational machinery utilized in this thesis and can be skipped by those who are familiar with computational hydrodynamics. In Chapter 3, I develop an analytic model for a SN expanding in a constant density medium (i.e. the ISM) and test my numeric code against this solution. In Chapter 4, I develop models for stellar groups and an idealized analytic solution to test against. Chapter 5 combines models from the two previous chapters to produce simulations of SN exploding in stellar groups. Finally, in Chapter 6 I discuss possible future works and the limitations of the models presented in this thesis.

2

Numerical Methods and Physical Ingredients

2.1 Hydrodynamics

Hydrodynamics is the study of the motion and flow of fluids. Fluids are characterized by their weak-to-nonexistent restoring forces. That is, once a fluid experiences a disturbance or deformation it will continue to deform until frictional effects have removed all the kinematic energy from the system. Additionally, fluids have trouble supporting shear stresses[1], with inviscid fluids completely incapable of supporting shear stresses. Gases, plasmas, and liquids all exhibit these qualities and therefore can be studied as hydrodynamic systems.

Each of the three phases listed above is distinct. Liquids are (mostly) incompressible, i.e. they maintain the same density and volume under various pressures. Gases and

[1]Shear stresses are easily visualized on the surface of a cube as a force that acts tangent to one of the faces.

plasmas may, however, change their density and volume in a manner which conserves mass. Unlike gases, plasmas contain ionized material that is affected by both electric and magnetic fields. Plasma effects on the scale of stellar clusters are, however, negligible allowing flows to be accurately modeled by hydrodynamics.

The motion of all hydrodynamic fluids can be described by the Navier-Stokes equations, which take into account viscosity. Fortunately, most astrophysical fluids have such extremely low densities and long interaction times between particles that viscosity is negligible[2]. By removing viscosity the Navier-Stokes equations can be reduced to the Euler equations:

$$\frac{\partial \rho}{\partial t} + \bigtriangledown \cdot (\rho \mathbf{v}) = 0 \qquad \text{(mass conservation)} \tag{2.1}$$

$$\frac{\partial \rho \mathbf{v}}{\partial t} + \bigtriangledown \cdot (\rho \mathbf{v} \otimes \mathbf{v}) + \bigtriangledown P = \rho \mathbf{g} \qquad \text{(momentum conservation)} \tag{2.2}$$

$$\frac{\partial \rho E}{\partial t} + \bigtriangledown \cdot \left[(\rho E + P) \mathbf{v} \right] = \rho \mathbf{v} \cdot \mathbf{g} \qquad \text{(energy conservation)} \tag{2.3}$$

The variables in these equations are defined as follows: ρ is the fluid density, $\mathbf{v}$ is the velocity, $\mathbf{v} \otimes \mathbf{v}$ is the tensor quantity $v_i v_j$, P is the pressure, E is the sum of the internal energy ϵ and kinetic energy per unit mass,

$$E = \epsilon + \frac{1}{2} |\mathbf{v}|^2 \tag{2.4}$$

$\mathbf{g}$ is the acceleration due to gravity, and t is time.

Conservation of momentum (Eq. 2.2) is a three dimensional vector equation, bringing our total number of equations to five. There are, however, six unknowns. Therefore,

[2] A notable exception are accretion discs, where viscosity and turbulence play important roles, however these will not be considered in this thesis.

it is necessary to introduce an equation relating pressure and density. The most widely used equation of state (and the one used throughout this thesis) is

$$P = (\gamma - 1)\,\rho\epsilon \tag{2.5}$$

or equivalently for an adiabatic ideal gas (see Appendix A for more details),

$$P \propto \rho^{\gamma} \tag{2.6}$$

where γ is the ratio of specific heats:

$$\gamma \equiv C_P / C_V. \tag{2.7}$$

2.2 Overview of Computational Methods

The astrophysical computational fluid dynamics community is divided between two main numeric methods: Eulerian and Lagrangian. Lagrangian methods work by following fluid parcels as they move. This would be like sitting in a boat drifting down river and determining how the boat will move. Eulerian methods track the fluid with respect to some static coordinate system, analogous to standing on the side of a river bank and watching the river flow by a particular spot. One particularly effective Eulerian method makes use of an adaptive mesh refinement (AMR) criteria. AMR methods first set up a dynamic grid akin to a piece of graph paper which is capable of changing grid spacing. This grid adapts to the fluid inside of it so that some regions have more compact grid-lines than other regions. Every block in this grid contains a small "parcel" of fluid described by a set of physical properties

(e.g. pressure, density, velocity, and temperature) and can interact with the fluid in adjacent blocks. A parameter that changes rapidly in space will cause each block nearby to be divided into smaller blocks. This allows for a closer look at shocks and other interesting phenomena without wasting computational power on regions where nothing is happening. The AMR approach allows for a broad range of densities to be resolved without over-resolving denser regions. Additionally, AMR is well suited for capturing shocks because the dynamic grid is capable of highly refine shocks without over refining the rest of the computational volume, making it well suited for studding the interactions between supernovae and stellar groups.

2.3 FLASH and AMR

I used the hydrodynamics, AMR code FLASH version 3.2 to solve the flow equations. This FORTRAN 90 code was written by The Center for Astrophysical Thermonuclear Flashes at the University of Chicago. The center's primary goal is to advance the understanding of a broad spectrum of complex phenomena that involve thermonuclear flashes, including X-ray bursts, classical novae and supernovae. This makes FLASH a very flexible code, ideal for the calculations presented here.

In order to accommodate such a wide variety of problems, FLASH has two important design features. First FLASH is a parallel code. Using the portable Message Passing Interface (MPI), FLASH is able to run calculations in parallel on several processors, speeding up complex calculations. Second, FLASH is written in a hierarchical modular fashion, allowing the user to pick and choose desired modules for each simulation. Because the modules are hierarchical, the user only has to choose the specific top level modules best suited for their simulation and FLASH will automatically determine the best base modules

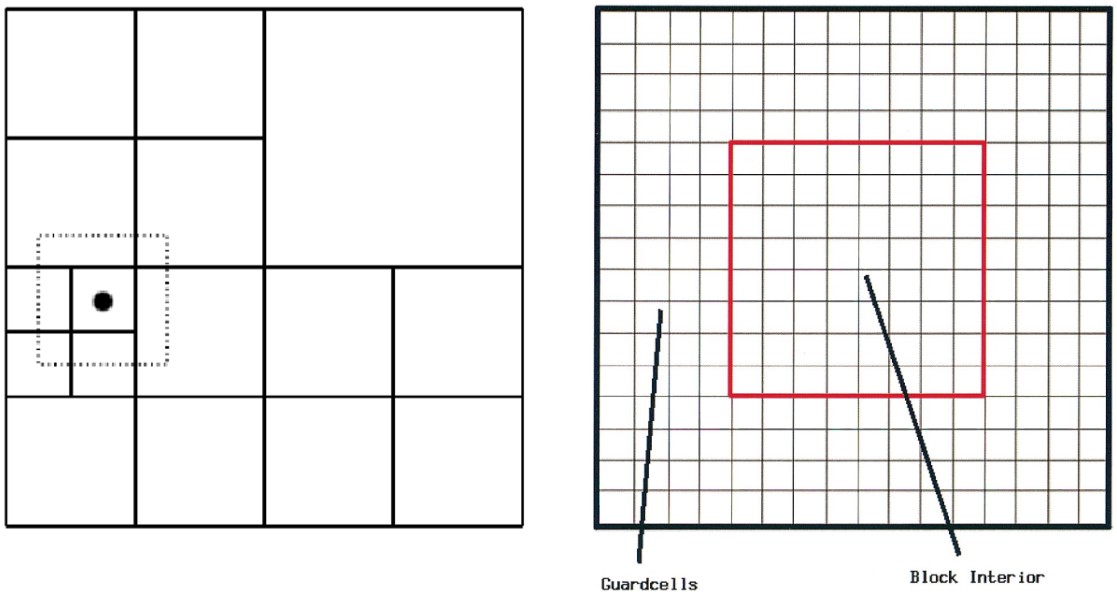

Figure 2.1 *Left panel*: A representation of how FLASH refines its adaptive mesh in a two dimensional computational volume (taken from FLASH 2009). Each square made of solid lines represents a block. Each of these blocks, regardless of their size, perform similar amounts of computation. The dotted lines enclose the block in which PARAMESH's refinement criteria is met. The blocks are different sizes because PARAMESH is refining the adaptive grid to better resolve a fluctuation in the fluid represented by the black dot. *Right panel*: The static internal structure of a single block (taken from Fryxell et al. 2000). Each square represents a cell which stores the fluid parameters averaged over the cell's volume. The cells within the red square are interior cells, those outside the red box are guard cells. The actual number of each type of cell depends on the interpolation method. The setup shown here is used when the piecewise parabolic method is used.

and add them during compilation.

Arguably the most essential and most used module is the hydrodynamics module. With its roots stemming from the PROMETHEUS code (Fryxell et al. 1989), this module solves the Euler equations (Equations 2.1-2.3) for a compressible inviscid gas-system in up to three spatial dimensions.

2.3.1 The Grid and Refinement

FLASH uses adaptive mesh library PARAMESH for grid placement and refinement. The PARAMESH Library is composed of several subroutines that are the heart of the adaptive mesh; it controls everything from grid refinement/derefinement to allocating the subsidiaries of this dynamic grid to different processors. Each of these subsidiary units is called a block (see left panel of Figure 2.1). Each block is itself composed of a static grid of cells which come in two types: interior cells and guard cells. As the names might imply, interior cells are located in the center of the block and the guard cells are located toward the outside of each block (see Figure 2.1). How exactly this is executed depends on the interpolation method used to determine information between cell centers. For the most used interpolation method (discussed in the next section), FLASH uses 16 cells in each dimension. The center eight cells belong to the blocks interior while the eight perimeter cells (four on each side) are guard cells. This is portrayed in two dimensions by the right panel of Figure 2.1.

Guard cells are used to get information from adjacent blocks. If a block and all of its neighboring blocks have the same refinement level the the guard cells simply copy the information from the interior cells of adjacent blocks. If there is a difference in refinement levels, then a linear interpolation method is used to fill the guard cells.

PARAMESH regulates the block structure in hierarchical fashion. The computational volume is first broken up into an arbitrary number of equally sized blocks determined by the user. These blocks form the base of the hierarchy, and when refinement occurs these blocks become parent blocks to a new level of sub-blocks or child-blocks. Each child block inherits information from its parent block and then acts as a standard block, even possibly

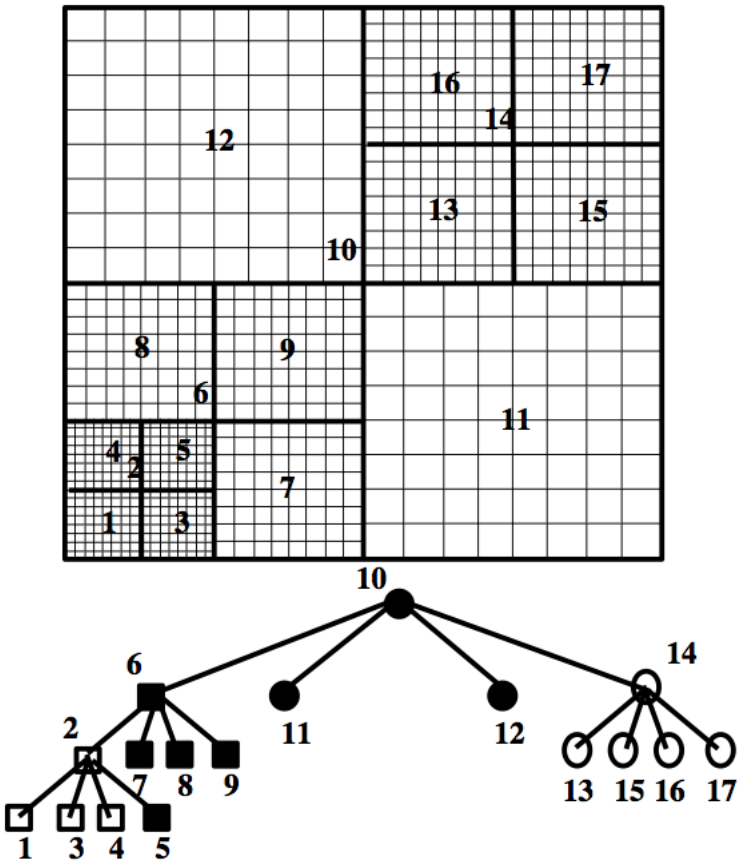

Figure 2.2 The grid above is similar to figure 2.1. Blocks have bold outlines and the interior cells of the blocks are shown using lighter thiner lines (guard cells are not shown). There are three different sizes of blocks corresponding to three levels of refinement. Each level is half the size in each dimension as the previous level. Each block is also numbered; note that blocks 2, 6, 10 and 14 are parent blocks, that is, they each contain blocks of their own. These numbered blocks follow a hierarchical structure shown in the tree below the grid. showing which child blocks belong to each parent block. The tree illustrates the inheritance from parent blocks to child blocks. The shape and shading in this tree signifies that different blocks are computed on different processors.

becoming a parent block with its own sub-blocks. The block structure follows three important rules: 1) When a block refines it must be sub-divided into child blocks that have half the size in each spatial dimension. 2) The child blocks must be nested in their parent block in such a way that there is no overlap between child blocks and that the child blocks combined fill the entire parent block. 3) Adjacent blocks cannot differ by more than one refinement level. Rules 1 and 2 ensure that parent blocks are composed of 2^d child blocks, where d is the number of spatial dimensions used in the simulation. See Figure 2.2 for a two dimensional illustration of the hierarchical block structure.

Eventually the iterative process of forming child blocks will run into the maximum refinement level chosen by the user at which point no more subdivisions can occur. This is a necessary precaution, as without this setting, the grid could refine indefinitely causing FLASH to run out of available processors.

To determine when to refine a block PARAMESH uses a modified second derivative test based on the work by Löhner (1987). This test is defined as follows in one dimension

$$E_i = \frac{|u_{i+1} - 2u_i + u_{i-1}|}{|u_{i+1} - u_i| + |u_i - u_{i-1}| + \epsilon\left(|u_{i+1}| + 2\,|u_i| + |u_{i-1}|\right)} \tag{2.8}$$

where u_i is the value of a fluid variable in the cell being tested and u_{i+1} and u_{i-1} are the values of the same variable in the adjacent cells. By default only density and pressure are checked by equation (2.8) but other variables may be used as well. The parameter ϵ has a default value of 0.01 and acts as a filter to prevent refinement on small ripples. Let E_{refine} and E_{derefine} be error values that correspond to refinement and derefinement respectively. If a block contains at least one cell with $E_i > E_{\text{refine}}$ then the block will refine. Conversely,

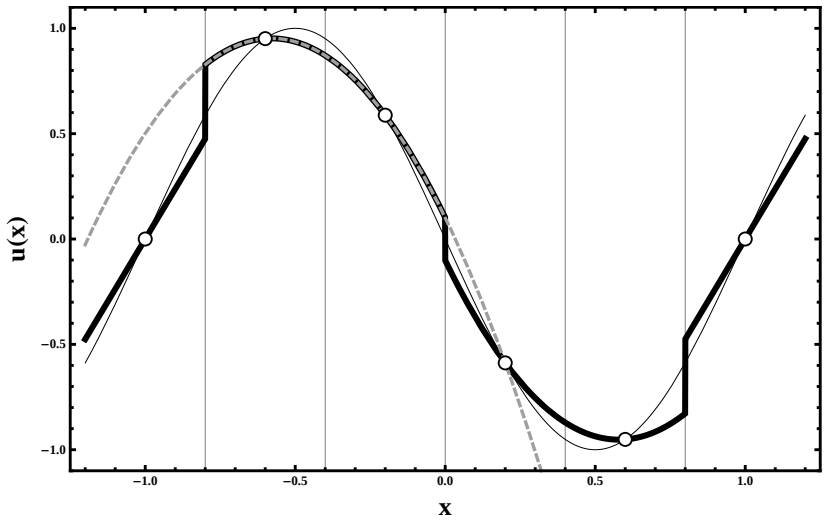

Figure 2.3 Piecewise Parabolic Method Diagram. The figure shows the results of a basic PPM interpolation method (bold black curve) compared to the function that it is approximating (thin black curve) in one dimension (recreated from Laney 1998). The PPM method uses multiple parabola as an approximation, one of which is illustrated here (dashed gray curve). $u(x)$ is the value of some fluid parameter along the x axis, such as density. For this example $u(x) = \sin(\pi x)$ and there are six points which are used for interpolation (open circles). In FLASH these correspond to the center of six cells, which are separated by vertical gray lines here.

if all the cells in a block have $E_i < E_{\text{derefine}}$ then the block will derefine. The parameters E_{refine} and E_{derefine} have default values of 0.8 and 0.2 respectively but can be chosen by the user.

2.3.2 Interpolation and Propagation of Information

Piecewise Parabolic Method. Interpolating fluid parameters between cell centers allows FLASH to gain accuracy at the cost of computational time, however this is well worth the price. The typical interpolation method used by FLASH, and the one used for the calculations presented in this thesis, is the piecewise parabolic method (PPM). This method uses a paraboloid to describe how fluid parameters vary over each cell. The most simplistic one dimensional PPM method determines the interpolation for a cell by choosing a parabola

that goes through the cell and two of the four cells closest to it. If we let x_i be the position for the center of the cell being examined and let x_{i+1} and x_{i+2} be the neighbors to the left and x_{i+1} and x_{i+2} be the neighbors to the right, then the interpolating quadratic will pass trough one of the following three set of points: $\{(x_{i-2}, u_{i-2}), (x_{i-1}, u_{i-1}), (x_i, u_i)\}$, $\{(x_{i-1}, u_{i-1}), (x_i, u_i), (x_{i+1}, u_{i+1})\}$, $\{(x_i, u_i), (x_{i+1}, u_{i+1}), (x_{i+2}, u_{i+2})\}$, where u_j is the value of the fluid variable at x_j. This simplistic method is demonstrated in Figure 2.3.

At first glance, the fact that the interpolating function is discontinuous might seem to be a disadvantage, but it is vital to capturing discontinuities in the fluid such as a shock wave. In fact, FLASH uses additional computation to contain these types of discontinuities to as few cells as possible. Another improvement that FLASH makes over simple PPM methods is that it tries to preserve monotonicity, i.e. if a fluid parameter is monotonic over a region of cells then FLASH tries to preserve this attribute in the interpolating function, thereby preventing the introduction of artificial oscillations in the fluid. Without this improvement contact discontinuities could expand, introducing errors into the computations such as artificial dissipation. These additions make the PPM method used by FLASH an efficient and highly accurate second order code.

Riemann Problem. Because FLASH discretizes fluids into cells it needs a mechanism for adjacent cells to communicate. Adjacent cells act like a tube containing a diaphragm separating fluids with different densities, pressures, etcetera. Communication would happen when the diaphragm is suddenly and instantaneously removed. This analogy restricts the velocity of the fluid on both sides of the tube to zero, but cells in FLASH do not have this restriction. The Riemann problem describes how the fluid in this more general "tube" evolves. There exists an analytical expression relating the evolved fluid to its initial parame-

ters (See Laney 1998, for a derivation of this solution), however inherent complexities of this relation require it to be solved via root-finding methods. The results from this calculation are used to determine how adjacent cells interact.

2.4 Plan for Utilization of Computational Framework

Now that we have developed a framework necessary to accurately calculating the motions of fluids, we are in a position to simulate the hydrodynamical evolution of SNe evolving within complex stellar wind interacting groups. However, before we embark in such a daunting task, it is useful to start with simpler versions of the problem and then progressively increase the level of complexity of our numerical framework. For this reason, in the section that follows we first simulate the evolution of SN remnant in a uniform background; conveniently this problem has an analytic solution and is a standard test for numerical codes. Following this we will focus on simulating the hydrodynamical conditions present within a massive stellar group environment. Then finally we will combine these two numerical descriptions, which will allow us to simulate SNe evolving in complex, wind-shocking environments.

3

Supernova Remnants in Constant-Density Media

Now we focus on understanding the simplest scenario for the evolution of SNRs. In this section I develop both analytic and computational frameworks to analyze the evolution of a spherically symmetric SNR evolving in a constant density medium, e.g the ISM.

The analytic solution to a point source explosion evolving through a constant density medium, analogs to a SNR, was developed independently by Sedov (1946, 1959) and Taylor (1950). The Sedov-Taylor solution was derived by noting that once the mass swept up by the shock is equivalent to the mass involved in the initial explosion, there are only four variables involved in the problem: E, the energy of the explosion; ρ_0, the ambient density; R_s, the radius of the shock wave; t, the time elapsed since the explosion. Therefore the following relation must hold:

$$R_s \propto E^{\alpha} \rho_0^{\beta} t^{\gamma} \tag{3.1}$$

where α, β, and γ are exponents to be determined. If we look at the dimensionality of these variables it is clear that α, β and γ can each only take one value, resulting in

$$R_s = \zeta \left(\frac{E t^2}{\rho_0} \right)^{1/5} \quad \text{with the proportionality constant } \zeta \sim 1. \tag{3.2}$$

See Appendix B for a derivation of the scaling relationship and an expression for ζ. For supernovae it is useful to write this equation using typical parameters

$$R_s = 5.91 \text{ pc } \times \left(\frac{E_{\rm SN}}{10^{51} \text{ ergs}} \right)^{1/5} \left(\frac{\rho_0}{10^{-24} \text{ g cm}^{-3}} \right)^{-1/5} \left(\frac{t}{1000 \text{ yr}} \right)^{2/5} \tag{3.3}$$

By using the dimensionless radius $x = \dfrac{r}{R_s(t)}$, the spherically symmetric Euler equations reduce to system of ordinary differential equations which can be solved easily and accurately by a standard numeric integration procedure such as Runge-Kutta (see Appendix B).

To reproduce the Sedov-Taylor solution in FLASH, all that needs to be done is to set a high pressure region in the middle of the computational volume and let it evolve according the the Euler equations. A snap shot of this simulation as well as a comparison between FLASH and the analytic solution is shown in Figure 3.1. With eight levels of refinement there is good agreement between FLASH and the Sedov-Taylor solution, signifying that the code works and that it is capable of accurately capturing shocks. There is a small discrepancy between the FLASH simulation and and the analytic solution at the shock, this is because shocks tend to get smoothed over a few blocks.

While this is a useful test, this setup only provides a useful description for SNR evolving in an homogeneous environment. Thus for this model to be valid, inhomogeneity length-scales must be much smaller than the Sedov scale. As I argue in the preceding

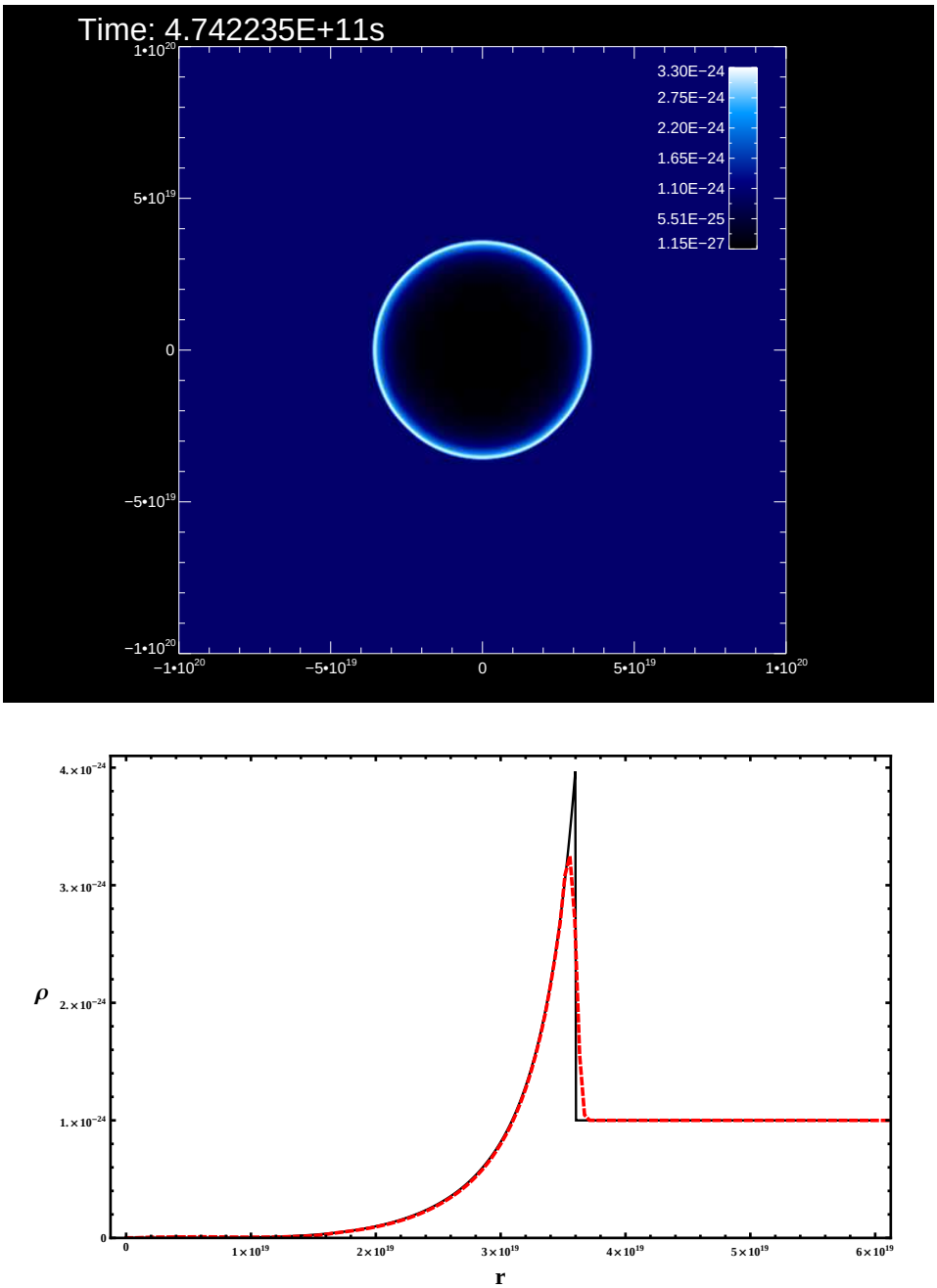

Figure 3.1 *Top frame*: Snapshot of three dimensional simulated SN. The snapshot is a slice through the xy plane of the simulation 15 kyr into the simulation. This FLASH simulation started with a point source explosion with energy 10^{50} ergs in an ambient medium with a density of 10^{-24} g cm^{-3} and a pressure of 10^{-12} ergs cm^{-3}. Eight levels of refinement were used in this simulation. *Bottom frame*: Comparison between FLASH and the Sedov-Taylor solution. Density verses radius is plotted for the analytic solution (black line), and for the FLASH simulation (red dashed line).

chapter, SNR evolving in stellar groups need a more detailed model description as the mean separation between stars is significantly smaller than the Sedov length scale.

4

Environments in Stellar Groups

The morphology and dynamics of young SNRs depend on the distribution of the ambient medium and on the structure of stellar ejecta. However, all models share two characteristics: an outer shock (blast wave) propagating into the ambient medium and an inner (reverse) shock propagating into the stellar ejecta. In the absence of characteristic scales in both the stellar ejecta and in the ambient medium, self-similar, spherically symmetric solutions exist (such as those described in the previous chapter), and they are widely used to interpret observational data on young SNRs. However, hydrodynamical instabilities and characteristic scales often exist in the external medium which necessitates the use of hydrodynamical models. In this chapter we examine the characteristic scales and hydrodynamical structures inherent to massive stellar group associations.

4.1 Idealized Stellar Group

The goal of my thesis is to understand the interactions between supernovae and the winds in stellar groups. Therefore, understanding the environments in and around isolated

stellar groups is vital. Stellar groups are complex entities which can contain a few stars to 10^5 stars, each expelling mass in the form of stellar winds[1]. These winds interact and create standing shocks throughout the cluster. While this creates a very complex environment, it is possible to obtain analytic functions which describe stellar groups using simplifying assumptions.

The idealized stellar group presented here (developed by Cantó et al. 2000) is spherically symmetric and contains N stars equally spaced within the group or cluster radius R_c resulting in the following number density:

$$n = \frac{3N}{4\pi R_c^3} \tag{4.1}$$

Additionally, we neglect gravitational forces as they are negligible on interstellar scales, leaving the only forces as the one exerted by stellar winds. For now we choose stars such that they have identical identical wind parameters, i.e. that have the same mass loss rates $\dot{M}_w$ and (terminal) wind velocities v_w. To make analytic calculations we "smooth" all the stars with in the cluster radius making the cluster perfectly homogeneous. Additionally, we assume that the stellar group is in a steady state. These assumptions allow us to integrate the mass conservation equation (Equation 2.1) over a sphere of arbitrary radius $r < R_c$

[1]By stellar groups I mean both clusters and associations as mentioned in Section 1.3

yielding

$$\iiint_V \bigtriangledown \cdot (\rho \mathbf{v})\ dV = -\iiint_V \frac{\partial \rho}{\partial t}\, dV$$

$$\oiint_S \rho \mathbf{v} \cdot d\mathbf{S} = n\dot{M}_w \iiint_V dV$$

$$4\pi r^2 \rho v = \frac{4}{3}\pi r^3 n\dot{M}_w, \tag{4.2}$$

which reduces to

$$\rho = \frac{n\dot{M}_w r}{3v} \tag{4.3}$$

If $r \geqslant R_c$ we obtain

$$\dot{M} \equiv \frac{4}{3}\pi R_c^3 n\dot{M}_w = 4\pi r^2 \rho v \tag{4.4}$$

We apply similar techniques on the energy conservation equation (Equation 2.3) to obtain

$$4\pi r^2 \rho v \left(\frac{1}{2}v^2 + \epsilon + \frac{P}{\rho}\right) = \frac{4}{3}\pi r^3 n\dot{M}_w \frac{v_w^2}{2} \tag{4.5}$$

By utilizing the equation of state (Equation 2.5) we can remove ϵ from this equation:

$$4\pi r^2 \rho v \left(\frac{1}{2}v^2 + \frac{\gamma}{\gamma - 1}\frac{P}{\rho}\right) = \frac{4}{3}\pi r^3 n\dot{M}_w \frac{v_w^2}{2} \tag{4.6}$$

Dividing this relationship by Equation 4.2 yields

$$\frac{1}{2}v^2 + \frac{\gamma}{\gamma - 1}\frac{P}{\rho} = \frac{1}{2}v_w \tag{4.7}$$

We can write this in terms of the sound speed (c_s) for an adiabatic fluid

$$c_s^2 = \gamma \frac{P}{\rho} \tag{4.8}$$

giving

$$c_s^2 = \frac{\gamma - 1}{2} \left(v_w^2 - v^2 \right). \tag{4.9}$$

Now lets examine the one dimensional momentum conservation equation:

$$v \frac{\partial \rho}{\partial t} + \rho v \frac{\partial v}{\partial r} + \frac{\partial P}{\partial r} = 0$$

Utilizing $\frac{\partial \rho}{\partial t} = n\dot{M}_w$ we get

$$n\dot{M}_w v + \rho v \frac{\partial v}{\partial r} + \frac{\partial P}{\partial r} = 0$$

and finally using Equation 4.8 we arrive at

$$n\dot{M}_w v + \rho v \frac{\partial v}{\partial r} + \frac{1}{\gamma} \frac{\partial}{\partial r} \left(\rho c_s^2 \right) = 0 \tag{4.10}$$

We can now combine Equations 4.3, 4.9 and 4.10 to obtain

$$\left[\frac{(\gamma - 1)\, v_w^2 - (\gamma + 1)\, v^2}{(\gamma + 1)\, v_w^2 + (5\gamma + 1)\, v^2} \right] \frac{dv^2}{v^2} = 2 \frac{dr}{r} \tag{4.11}$$

Integrating this equation results in

$$\boxed{u \left[1 + \frac{5\gamma + 1}{\gamma + 1} u^2 \right]^{-(3\gamma+1)/(5\gamma+1)} = Ax,} \tag{4.12}$$

where u and x are the dimensionless variables

$$u \equiv \frac{v}{v_w} \text{ and } x \equiv \frac{r}{R_c}, \tag{4.13}$$

and A is an integration constant. From this equation it is clear that $u = 0$ when $x = 0$. Also, note that because Equation 4.3 is only valid when $r < R_c$ ($x < 1$), Equation 4.12 is only valid inside the cluster radius.

For $x > 1$ we instead combine and integrate Equations 4.4, 4.9 and 4.10 in a similar fashion to obtain

$$\boxed{u\left(1-u^2\right)^{1/(\gamma-1)} = \frac{B}{x^2}} \tag{4.14}$$

where b is an integration constant. As $x \to \infty$ the left-hand side approaches resulting in two possibilities for u: $u \to 0$ (asymptotically subsonic flow) and $u \to 1$ (asymptotically supersonic flow). For the subsonic solution the limiting values of the density, sound speed and pressure are

$$\rho_{sub}(\infty) = \frac{\dot{M}}{4\pi B R_c^2 v_w} \tag{4.15}$$

$$c_{s,sub}^2(\infty) = \frac{\gamma-1}{2} v_w^2 \tag{4.16}$$

$$P_{sub}(\infty) = \frac{\gamma-1}{2\gamma} \frac{\dot{M} v_w}{4\pi B R_c^2}. \tag{4.17}$$

The corresponding solutions for the supersonic case are

$$\rho_{sup}(\infty) = c_{s,sup}^2(\infty) = P_{sup}(\infty) = 0 \tag{4.18}$$

For the subsonic case the limiting values of pressure and density should correspond to the pressure (P_∞) and density (ρ_∞) of the ISM (or other ambient medium). If we set $P_{sub}(\infty) = P_\infty$ we can use Equation 4.17 to obtain

$$B = \frac{\gamma - 1}{2\gamma} \frac{\dot{M} v_w}{4\pi R_c^2 P_\infty}. \tag{4.19}$$

Using this and Equation 4.14 we can get an implicit expression for the velocity (u_1) at the outer edge of the boundary ($x = 1$):

$$u\left(1 - u^2\right)^{1/(\gamma-1)} = B. \tag{4.20}$$

By using u_1 in Equation 4.12 we get the following expression for A

$$A = u\left[1 + \frac{5\gamma + 1}{\gamma + 1} u^2\right]^{-(3\gamma+1)/(5\gamma+1)}. \tag{4.21}$$

By examining Equation 4.19 the maximum value for B can be determined:

$$B_{max} = \left(\frac{\gamma - 1}{\gamma + 1}\right)^{1/2} \left(\frac{2}{\gamma + 1}\right)^{1/(\gamma-1)} \tag{4.22}$$

which occurs at

$$u = \left(\frac{\gamma - 1}{\gamma + 1}\right)^{1/2} \tag{4.23}$$

Thus Equations 4.17 and 4.22 give the supersonic condition: if

$$P_\infty < \frac{\gamma - 1}{2\gamma} \frac{\dot{M} v_w}{4\pi B_m a x R_c^2} = \frac{1}{\gamma} \left(\frac{\gamma - 1}{\gamma + 1}\right)^{1/2} \left(\frac{\gamma + 1}{2}\right)^{\gamma/(\gamma-1)} \frac{\dot{M} v_w}{4\pi R_c^2} \tag{4.24}$$

then the solution must be supersonic, requiring that A an B reach their limiting values:

$$A = \left(\frac{\gamma-1}{\gamma+1}\right)^{1/2}\left(\frac{\gamma+1}{6\gamma+2}\right)^{(3\gamma+1)/(5\gamma+1)} \tag{4.25}$$

$$B = \left(\frac{\gamma-1}{\gamma+1}\right)^{1/2}\left(\frac{2}{\gamma+1}\right)^{1/(\gamma-1)} \tag{4.26}$$

4.2 One Dimensional Idealized FLASH model

It is simple to implement the idealized model presented above in a one dimensional FLASH simulation. By assuming that mass is continually injected homogeneously throughout the stellar group ($r \leqslant R_c$), it is clear that

$$\rho\left(r, t+dt\right) = \rho\left(r,t\right) + \frac{3\dot{M}}{4\pi R_c^3}dt = \rho\left(r,t\right) + n\dot{M}_w dt, \tag{4.27}$$

where dt is the time step taken in FLASH. In addition we need to ensure that momentum is conserved in each cell, requiring that

$$v\left(r, t+dt\right) = \frac{\rho\left(r,t\right)}{\rho\left(r,t+dt\right)}v\left(r,t\right) \tag{4.28}$$

Because the mass that is being injected into the cluster has velocity v_w the energy added to the system is $\frac{1}{2}n\dot{M}_w v_w^2 dt$. Recall that the energy per unit mass (E) is the sum of the internal energy ϵ and kinetic energy per unit mass (Equation 2.4)

$$E = \epsilon + \frac{1}{2}v^2.$$

This combined with Equations 4.27 and 4.28 gives

$$\begin{aligned}\epsilon\left(r,t+dt\right) &= E\left(r,t+dt\right)-\frac{1}{2}v^{2}\left(r,t+dt\right)\\ &= \frac{\rho\left(r,t\right)}{\rho\left(r,t+dt\right)}\left(\epsilon\left(r,t\right)+\frac{1}{2}v^{2}\left(r,t\right)\right)+\frac{1}{2}n\dot{M}_{w}v_{w}^{2}dt-\frac{1}{2}v^{2}\left(r,t+dt\right).\end{aligned} \tag{4.29}$$

Eventually a steady state is achieved where the outflow from the stellar group is equal to the injection of mass, at which point the simulation should produce the same results as the analytic solution.

I implemented this procedure with the following parameters:

$$N = 10 \tag{4.30a}$$

$$R_c = 2\times10^{18}\text{ cm} = 0.65\text{ pc} \tag{4.30b}$$

$$v_w = 600\text{ km s}^{-1} \tag{4.30c}$$

$$\dot{M} = 3.33\times10^{-5}\text{ M}_{\odot}\text{ yr}^{-1} \tag{4.30d}$$

$$\rho_{\infty} = 10^{-24}\text{ g cm}^{-3} \tag{4.30e}$$

$$P_{\infty} = 10^{-12}\text{ ergs cm}^{-3} \tag{4.30f}$$

$$\gamma = 5/3 \tag{4.30g}$$

giving a number density of

$$n = 2.9\text{ pc}^{-3} \tag{4.30h}$$

The results from this simulation closely match the analytic solution, with the velocity in complete agreement (see Figure 4.1). The density profile obtained by FLASH matches the analytic solution both inside the cluster radius and far from the origin, but

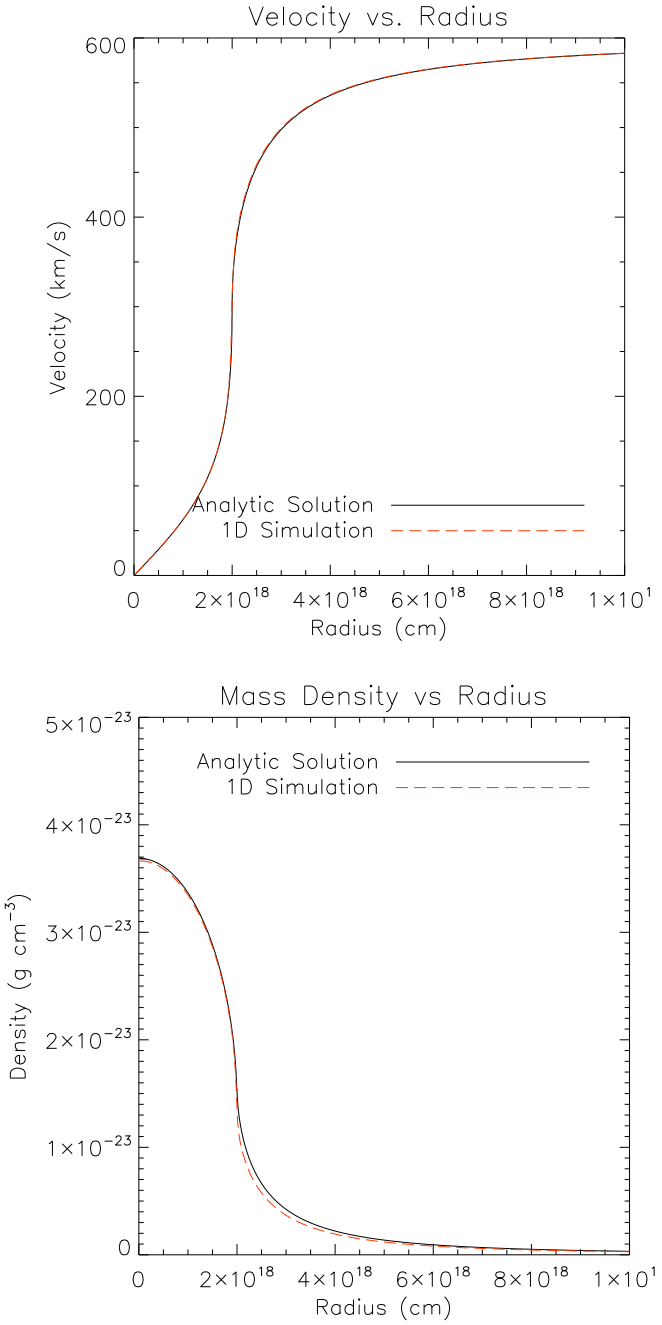

Figure 4.1 Plots of 1D FLASH code and analytic solution. Comparison of radial velocity (top panel) and density (bottom panel) profiles between the analytics solution developed by Cantó et al. (2000) (thin black curve) and the one dimensional FLASH code (thick dashed red line).

differs slightly just outside the cluster radius. Despite this minor discrepancy, the FLASH and analytic models are in good agreement.

4.3 Three Dimensional Stellar Group Models in FLASH

In reality, stellar groups are three dimensional entities with stars acting like discreet source terms and generally having different wind parameters. Thus, there are obvious differences between three dimensional simulations and the simple, one dimensional analytic solution derived by Cantó et al. (2000). In this section I develop two different types of 3D models for stellar groups. The first is still somewhat simplistic and was designed to match the analytic solution as closely as possible. The second attempts to accurately portray a more realistic stellar group.

4.3.1 Simplistic Model

The simple model contains N stars distributed within a radius R_c. These stars are modeled as spherical outflow boundaries with identical wind parameters $\dot{M}_w$ and v_w. The stars are distributed such that the radial distance from each star to the center of the cluster ($r_\star$) is chosen in the following manner.

$$r_\star = R_c \times p_{\text{top hat}}^{1/3} \tag{4.31}$$

where $p_{\text{top hat}}$ is a pseudo-random number between 0 and 1, which is generated with a top hat probability distribution, i.e. all numbers between 0 and 1 have an equal probability of occurring. This probability distribution was chosen so that the number density of stars

(n) becomes constant within R_c as $N \to \infty$, however different probability distributions can be used. If we only examine this model when the interactions between stars have reached a quasi-steady-state and the winds have filled the entire computational volume, then as $N \to \infty$ this model approaches the one dimensional idealized model.

I implemented this simple model with the same parameters used for the one dimensional model to make a direct comparison (see Figure 4.2). The configuration of stars generated by Equation 4.31 using the parameters mentioned are listed in Appendix C and will be referred to as the Cantó cluster from here on. In order to compare the three dimensional results to the one dimensional analytic solution, fluid parameters are averaged over spherical shells. This can be idealized as

$$f(r) = \frac{1}{4\pi r^2} \int_0^{2\pi} \int_0^{\pi} f(r, \theta, \phi)\, r^2 \sin(\theta)\; d\theta\, d\phi, \tag{4.32}$$

where f is an arbitrary fluid parameter. However, cells in flash are not infinitesimal, so in actuality, this is a discrete sum.

It is now possible to directly compare the density and velocity of the different models (see Figure 4.2). Inside the cluster radius, the density and velocity from the three dimensional FLASH calculation differ from the analytic and one dimensional FLASH solutions but are qualitatively in agreement. This is expected because with this new model we have introduced more structure and complexity, making the interior ($r < R_c$) much less homogeneous. Outside the cluster radius, there is good agreement between the three solutions which makes intuitive sense; as $r \to \infty$ the structure inside the cluster radius ceases to be important.

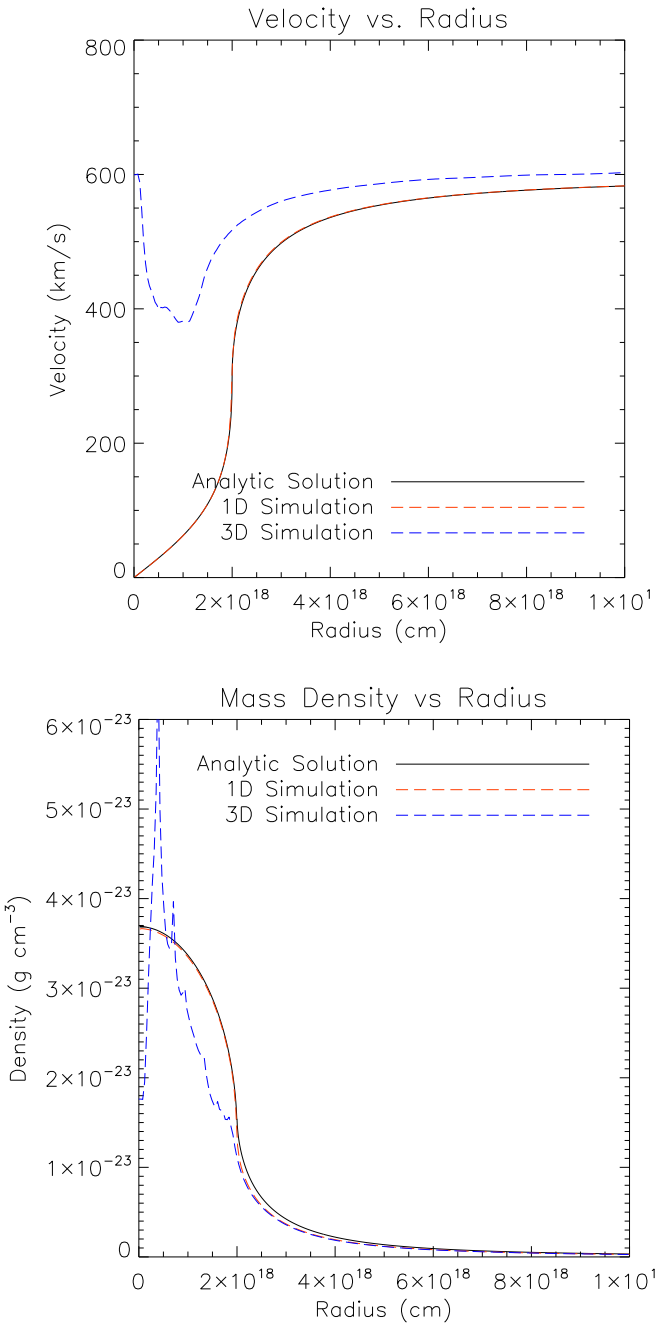

Figure 4.2 Plots of FLASH and analytic solution. Comparison of radial velocity (top panel) and density (bottom panel) profiles between the analytics solution developed by Cantó et al. (2000) (thin black curve), one dimensional FLASH code (thick dashed red line) and three dimensional FLASH simulation of the Cantó cluster (thick dashed blue line).

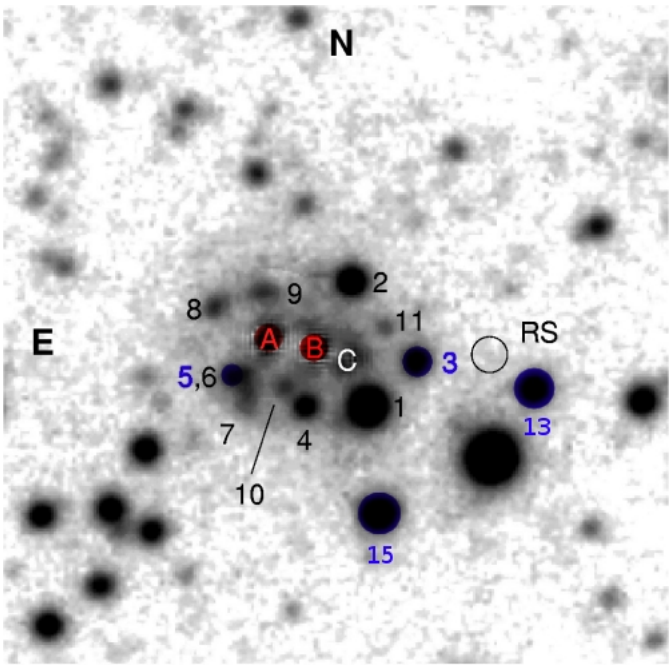

Figure 4.3 Image of the stellar group associated with the magnetar SGR 1900−14 (adapted from Vrba et al. 2000). The image is a 6.5 hr exposure in the I-band and captures approximately $45'' \times 45''$ of the sky. The colored stars (A, B, 3, 5, 13, 15) have been confirmed to be members of this association by Davies et al. (2009). The red stars (A,B) are red supergiants (RSGs), while 3 of the blue stars (3, 13, 15) are blue supergiants (BSGs). The remaining blue star (5) is an OB dwarf. The circle marked RS (radio source) is the approximate location of the magnetar SGR 1900−14.

4.3.2 Realistic Model

Next, I will create and examine a more realistic model for stellar groups based actual observations. I choose the stellar group discovered by Vrba et al. (2000) (see Figure 4.3) as a base for creating this model. This group is ideal to model because it has only a few massive stars, making it less computationally expensive. Additionally, this stellar group has been linked to the magnetar SGR 1900−14, meaning that a star in this cluster has likely exploded as a SN relatively recently (within the past 10 kyr).

To accurately model this stellar group, I used observational data from Davies et al. (2009) to determine the properties of the group and the stars within. First, I compared the

observed spectral type of each star identified in the association to observed wind parameters of similar stars from Repolust et al. (2004) and van Loon et al. (2005). The confirmed members of the group are three BSGs, two RSGs, and one OB main sequence star. The estimated distance between Earth and the stellar group have been determined to be $D = 12.5 \pm 1.7$ kpc by Davies et al. (2009), for the purpose of this paper I use $D = 14$ kpc as the distance in the hope that a greater spacing between stars will result in more noticeable interactions between a SN and the group. This distance allows us to convert the angular distances between stars (θ) into physical distances (d):

$$d \approx D\theta. \tag{4.33}$$

Thus we can now determine two of the spatial coordinates (x, y) for each star; for ease the center of the group (determined by the mean of spatial coordinates) is set to $(0, 0)$. To determine the z coordinate (the coordinate along the line of sight) of each star we used the following method:

$$z_\star = \frac{R_g}{2} \exp\left(-\frac{x_\star^2 + y_\star^2}{2r_p^2}\right) \times p_{\text{ Gauss}} \tag{4.34}$$

Where r_g is the radius of the stellar group (approximated by eye as 1 pc); $p_{\text{ Gauss}}$ is a pseudo-random number generated with a Gaussian distribution of unit standard deviation (although other probability distributions can be utilized); and $x_\star$, $y_\star$, and $z_\star$ are the coordinates of a star in the group. If the intrinsic radial distribution of this group is Gaussian, then this method roughly preserves the radial distribution of stars, mimicking a central concentration of massive stars.

In addition to the observed members of the group, there are likely members in the

main sequence that have evaded detection (Davies et al. 2009). Therefore, I have added two OB main sequence stars with radial positions from the center of the cluster ($r_\star$) generated by $R_g \times p_{\text{ Gauss}}$. Additionally this group has been observed post SN, prompting me to add a RSG at the origin $(0, 0, 0)$ as the SN progenitor. The progenitor position was chosen for both ease and to maximize interactions between the stars and a SN. The configuration of stars obtained by this method is listed in Appendix C and will be referred to as the Vbra group from here on out.

Unlike the Cantó cluster, the Vrba group has stars with different wind parameters. Therefore we need to determine the effective mass loss rate and wind velocity for each star ($\dot{M}_w$ and v_w respectively). These effective wind parameters are as follows:

$$\dot{M}_w = \sum_{i=1}^{N} \dot{M}_{w,i} \tag{4.35a}$$

$$v_w^2 = \sum_{i=1}^{N} \frac{\dot{M}_{w,i} v_{w,i}^2}{N \dot{M}_w}, \tag{4.35b}$$

producing $\dot{M}_w = 3.2 \times 10^{-5}$ $\text{M}_\odot$ yr^{-1} and $v_w \approx 600$ km s^{-1}. The only quantity missing to make a direct comparison is an outer radius (defined as R_c in the analytic model). The method by which the Vrba group was created makes R_c somewhat ambiguous, because the radial distribution of stars is based on a Gaussian profile with standard deviation R_g and thus has no well defined outer edge. However it makes intuitive sense that R_c and R_g are comparable, so I chose to let $R_c = 2R_g = 2$ pc $= 6.17 \times 10^{18}$ cm (this is certainly more reasonable than $3R_g$ with a group of 9 stars since they are most likely contained within this radius). Now we can compare the FLASH simulation of the Vrba group (after a quasi-steady-state has been reached; i.e. a few sound crossing times) to the analytic

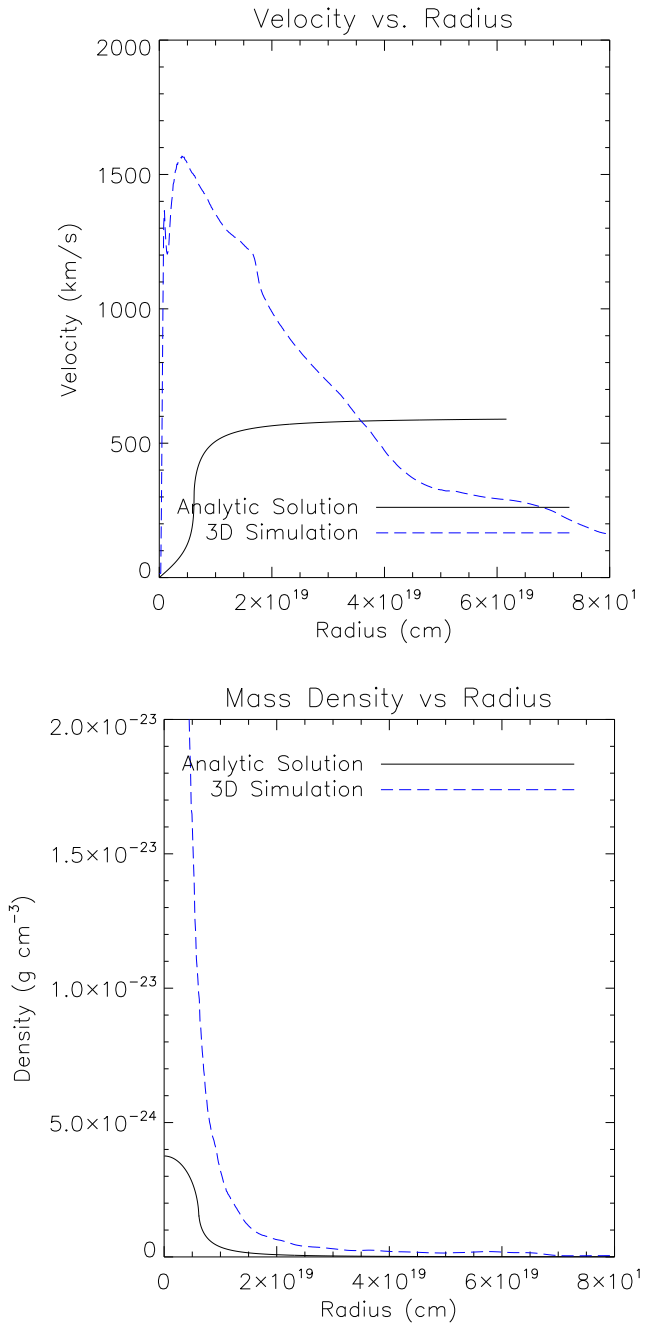

Figure 4.4 Plots of FLASH and analytic solution. Comparison of radial velocity (top panel) and density (bottom panel) profiles between the analytics solution developed by Cantó et al. (2000) (thin black curve) and three dimensional FLASH simulation of the Vrba group (thick dashed blue line).

solution (see Figure 4.4). The Vrba group simulation drastically different from the analytic model, signifying that this group breaks the assumptions made by Cantó et al. (2000). First, the Vrba group has stars with significantly different wind parameters. Second, the stars in the Vrba group are centrally concentrated as opposed to uniformly space. Finally, the number of stars is small for the one-dimensional approximation to be applicable. The marked differences between models seen in Figure 4.4 exemplifies the importance of three dimensional models.

4.3.3 Three Dimensional Structure

So far in my analysis of three dimensional simulation, I have only analyzed radial profiles, thus ignoring the complex structure created by these models. Next, I examine the simulations of the Cantó cluster and Vrba group as fully three dimensional simulations (See Figure 4.5).

Both simulated groups have several wind-wind interactions, creating multiple standing shocks. This highly irregular environment breaks the assumptions made in Chapter 3, requiring the evolution of SNe embedded in stellar clusters to be determined by numerical simulations.

Vrba Group (log density)

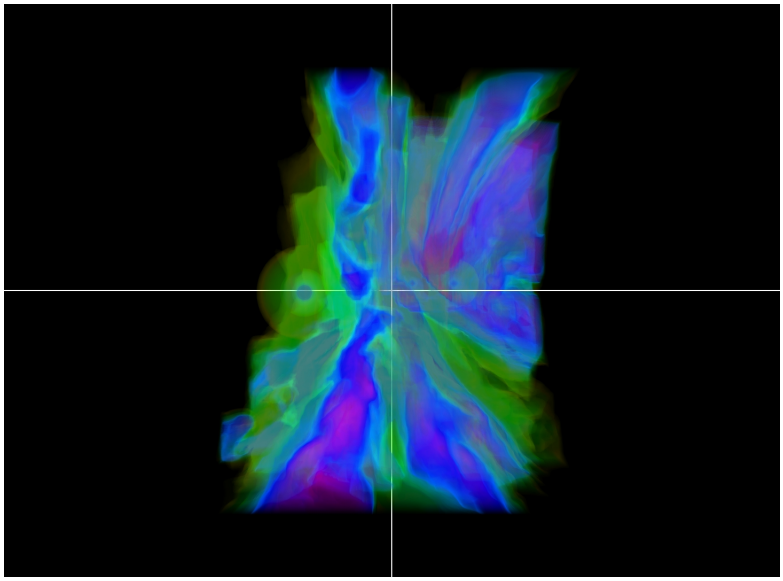

Cantó Cluster (log density)

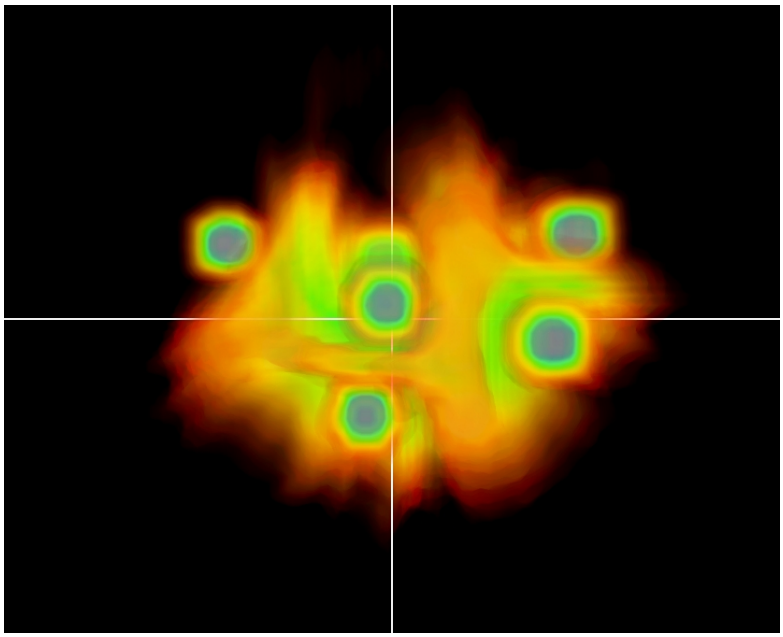

Figure 4.5 Simulation renderings of simulated groups in quasi-steady-state. *Top Panel*: three dimensional image of the Vrba group with the log of density shown, with purple corresponding to 10^{-20} g cm^{-3} and red corresponding to 10^{-26}. The purple vertical line near the center white line is a standing wind-wind shock.*Bottom Panel*: three dimensional image of the Cantó cluster with the linear density shown. For this cluster it is more enlightening to see linear density because there are no large density contrasts due to the uniformity of the stars. Red corresponds to 10^{-23} g cm^{-3} and purple corresponds to 10^{-22} g cm^{-3} . Several stars are visible as blue-purple balls.

5

Supernovae in Stellar Groups

Now that we have developed the framework to model the evolution of SNR as well as the complex environments of stellar groups, we can begin to model the expansion of SNR within these complex environments.

For the Vrba group, the star at the origin of the simulation is chosen as the progenitor. After we choose a star as the progenitor of the supernova, we replace it with a region of high pressure and density. The additional density is implemented to account for the ejecta (material from the progenitor that is swept up when the SN is created). This high pressure condition is implemented in the same way as the simulation of a SN evolving in a constant density medium. The difference is that we are now initiating the SN inside a stellar group. Thus, as the SN evolves it interacts with a more complex environment (See Figures 5.1, 5.2)

Based on these simulations, wind-wind shocks help confine the evolving SNR. There are two contributing factors that make this so. First these standing wind-wind shocks are much denser then the surrounding medium, slowing down the progression of the SN.

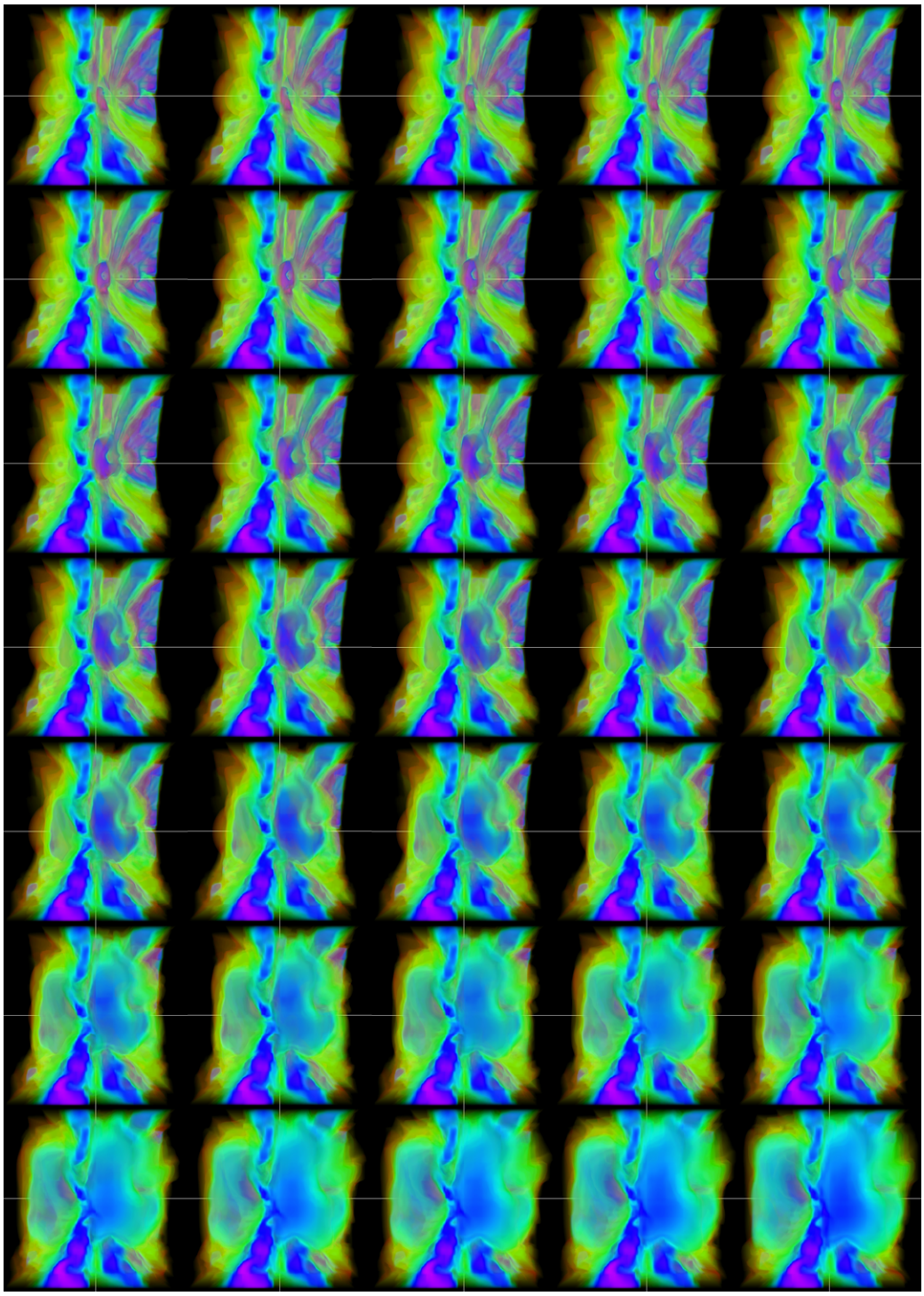

Figure 5.1 Time progression of the log of density as a SNR evolves within the Vrba group from 20 to 700 yr. The frames are ordered left to right, top to bottom. The time between adjacent frames is 20 yr, with log of density shown.

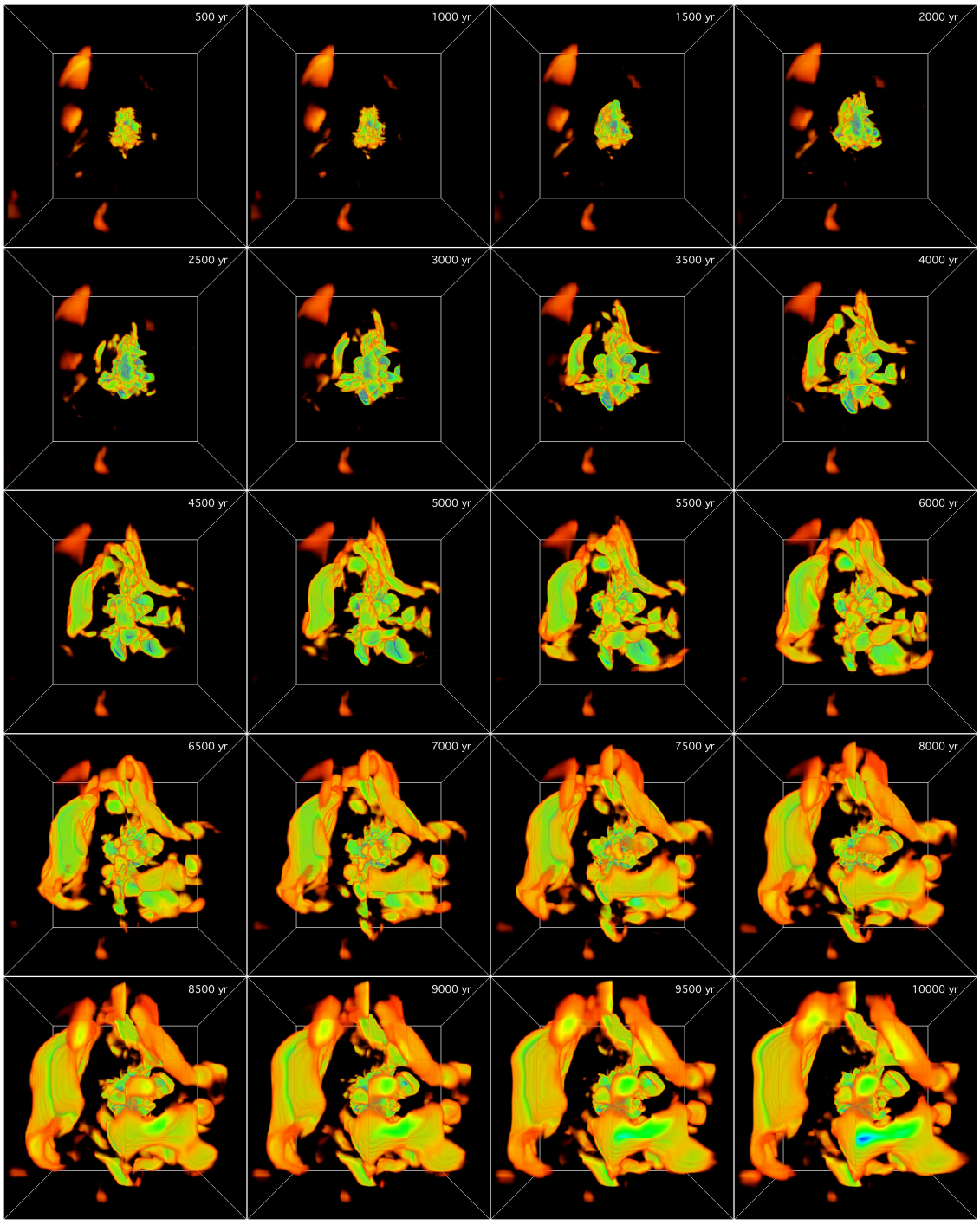

Figure 5.2 Time progression of the log of pressure as a SNR evolves through the environment created by the Vrba group. The frames are ordered left to right, top to bottom. The first frame is 500 yr after the initialization of the SN and the time between adjacent frames is 500 yr, with log of pressure shown. This figure has a different time scale then the previous one because it is zoomed out by a factor of ten. This figure shows high pressure regions expanding outward which correspond to the surface of the SNR

Secondly, the associated pressures in these regions push against the SNR. Not surprising, the vertical blue and purple standing shocks that are visible throughout Figure 5.1 seem to line up with the hole in the evolving pressure surface of the remnant (see Figure 5.2).

However, direct interactions with stellar winds of the individual stars appear to have a more localized effect, *punching holes* in the remnant. This is due to the associated ram pressure of the stellar winds, which can help disrupt and penetrate the surface of the evolving remnant, which results in the formation of a hole in the SNR as clearly seen in Figure 5.1.

Now that we have this information we can begin to understand how complex environments impede the evolution of SNe. With only one simulations it is difficult to understand what environmental parameters have the greatest influence on SNe evolution; fortunately, the framework that has been presented here can be easily expanded to explore the large complexity of the problem at hand.

6

Future Work and Limitations

The method developed in this thesis for modeling the evolution of SNe embedded in stellar groups, although novel, can be significantly improved. In what follows I will briefly describe ways in which I will improve the current model in the near future.

6.1 Microphysics

The most difficult task at present is to relate hydrodynamical modeling to observations. A few of the observables, such as expansion rates and thicknesses of the flow structures, can be relatively easily determined from the models. However, modeling radio and X-ray emission is in general difficult. Efforts to do so are still in their infancy because we still lack the understanding of how electrons are accelerated in SNR shocks. Very similar difficulties are encountered in modeling nonthermal X-rays. Thermal X-ray spectra are in principle easier to model, but in practice formidable. The reason for these difficulties is our poor understanding of a number of topics, such as the amount of electron heating in collisionless shocks, the detailed structure of SN ejecta, their clumping, the presence of the

nonhomogeneous circumstellar medium, and the presence of dust.

With the launch of *Chandra* we are able to peer deeper into the hearts of stars by examining the presence of strong lines of elements such as Si and S in the X-ray spectrum of SNRs. By observing these lines we are observing heavy-element enriched material produced deep within the exploded star offering us a unique opportunity to literally look into the stellar interior. This tantalizing possibility has always been the magnet for studies of young SNRs, but until now the poor quality of observational data hampered progress in this field. Thus in order to take advantage of these new observations, we need to intensify our efforts to better model the dynamics and the cooling mechanisms in a self-consistent framework.

6.2 Modeling the Birth of the Magnetar SGR 1900−14

By adding cooling processes to the dynamics presented in this work, it is possible to determine the detectability of a SNR that evolved from within a stellar group. The group associated with magnetar SGR 1900−14 is a prime candidate for this type of simulation. This magnetar has a spin down age of 1.3 kyr, suggesting that a CCSN occurred in the past few thousand years. However, there is absolutely no sign of a SNR despite multi-wavelength observation and the fact that the spin-down age of SGR 1900−14 is $\sim 7\%$ of the observability timescale for a SNR. This discrepancy is quite perplexing, and if our understanding of magnetars is correct then the environment provided by the group associated with SGR 1900−14 should significantly disturbed if not destroy the progenitor SNR within a few thousand years. In the near future, I seek to resolve this puzzle utilizing the methods presented in this thesis implemented with the addition of adequate cooling prescriptions.

6.3 The Environment of SNRs and Their Detectability

I hope that my thesis has provide the reader with a clear understanding of the important notion that the morphology and visibility of supernova remnants are determined largely by their circumstellar environments. The importance of the circumstellar medium in influencing the structure and evolution of SNRs was a recurring theme.

I began to appreciate that the evolution of SNRs was not a simple, one-dimensional path, that individual remnants may be in multiple, concurrent stages of evolution, and that multiple, different evolutionary paths probably exist. The importance of understanding all of the different thermodynamic and physical components of SNRs, including the relativistic plasma, was emphasized. I see promising applications for the code framework developed here to model a diverse range of SNe evolutions. I now leave you with some final thoughts about the diverse environments that SNe evolve in.

Since supernova remnants result from the impact of the supernova ejecta with circumstellar gas, the visibility of SNRs is highly biased in favor of those with massive progenitors, such as Cas A, which are concentrated in the disk of the Milky Way. Many young SNRs from massive progenitors are bright because the supernova ejecta are interacting with nearby gas expelled by the progenitor itself, presumably during a red supergiant stage. This circumstellar gas is likely to have mass comparable to that of the supernova debris and will not extend much further than a few parsecs. After several centuries, the blast wave from the supernova will pass through this relatively dense circumstellar gas.

But the interstellar medium beyond this relic red giant wind is also likely to have been highly disturbed by the progenitor evolution. For example, the stellar wind from a blue supergiant stage preceding the red supergiant stage could have displaced the interstellar gas

with an interstellar bubble of hot, low-density gas surrounded by a dense shell of radius $\sim$ 20 pc or more. If so, a supernova blast wave may remain nearly invisible for several thousand years, from the time it exits the relic red giant wind until it strikes the bubble wall. When it does, we will see a "mature" supernova remnant, such as the Cygnus Loop. In such a scenario, the actual age of the SNR may be considerably less than the kinematical age estimated from the radius of the filaments divided by the expansion velocity. Moreover, counts of supernova remnants as a function of age may have huge selection effects. Thus it is necessary to exercise extreme caution in inferring supernova rates from counts of mature and old SNRs.

Even more important, as we have argued here, is that most massive stars are found in clusters. Therefore, most CCSN will not be the first one in the vicinity but more likely will occur in a medium that has been highly disturbed by the action of previous supernovae. The typical lifetime of a massive star that is likely to end as a supernova (a few $\times 10^7$ yr) is not long enough for the interstellar medium to back-fill the cavity left by a previous supernova. An OB association will give rise to several supernovae in this interval. For example, even a relatively modest cluster such as the Pleiades should have already produced several supernovae. In a cluster, each subsequent supernova will revive the cavity left by the previous ones, causing the formation of a "superbubble" with diameter $\sim$ 100 pc or more. The superbubble interior may be quite irregular, containing high velocity filaments moving chaotically, as we see in the Vela Puppis region. Other prominent superbubbles in the Milky Way are those surrounding the Cygnus OB1 association, the Aquila supershell , and the Monogem Ring. We also see several superbubbles around OB associations in the Large Magellanic Cloud, showing us that the universe is full of complex environments.

Appendix A

Equation of State

In this section I show in detail that the equation of state (2.5) is equivalent to Equation 2.6 for an adiabatic ideal gas:

$$P = (\gamma - 1)\,\rho\epsilon \quad \Leftrightarrow \quad P \propto \rho^{\gamma} \quad . \tag{A.1}$$

A good starting point is the ideal gas law:

$$P = \frac{R}{\mu}\rho T \tag{A.2}$$

where μ is the average mass per particle, P is pressure, ρ is density, T is temperature, and R is a constant. A value for R/μ can be determined by examining the relation between the specific heats C_V and C_P. To determine this relation it is useful to start with the first law of thermodynamics:

$$dE = dQ - PdV \tag{A.3}$$

where E is the energy of the system, dQ is the change in heat, and V is volume. From this we can derive the definition of specific heat, i.e. the change in heat per change in temperature:

$$\begin{aligned} dQ &= dE + PdV \\ \frac{dQ}{dT} &= \frac{dE}{dT} + P\frac{dV}{dT}. \end{aligned} \tag{A.4}$$

If we constrain ourselves to a constant volume (i.e. $dV = 0$) then we get

$$C_V \equiv \left(\frac{dQ}{dT}\right)_V = \left(\frac{dE}{dT}\right)_V \tag{A.5}$$

where the parentheses with the subscript V signify that these derivatives at constant volume. Conversely, if we examine Equation A.4 at constant pressure then we get

$$C_P \equiv \left(\frac{dQ}{dT}\right)_P = \left(\frac{dE}{dT}\right)_P + P\left(\frac{dV}{dT}\right)_P. \tag{A.6}$$

The energy of an ideal gas is a function of temperature only, thus

$$\left(\frac{dE}{dT}\right)_V = \left(\frac{dE}{dT}\right)_P \tag{A.7}$$

and

$$C_P - C_V = P\left(\frac{dV}{dT}\right)_P. \tag{A.8}$$

We can determine the value of this derivative be examining the ideal gas law

(Equation A.2)

$$\frac{1}{\rho} = \frac{R}{\mu}\frac{T}{P}$$

at constant pressure

$$d\left(\frac{1}{\rho}\right) = dV = \frac{R}{\mu}\frac{dT}{P}$$

$$\left(\frac{dV}{dT}\right)_P = \frac{R}{\mu P}. \tag{A.9}$$

Thus

$$C_P - C_V = \frac{R}{\mu}. \tag{A.10}$$

If the fluid is adiabatic then $dQ = 0$ thus Equation A.3 reduces to

$$dE = -PdV \tag{A.11}$$

dividing and multiplying the left hand side by dT

$$\frac{dE}{dT}dT = -PdV$$

using the definition of C_V and the ideal gas law (Equations A.5 and A.2 respectively) we get

$$C_V dT = -\frac{R}{\mu}\rho T dV$$

$$C_V dT = -\frac{R}{\mu}\rho T d\left(\frac{1}{\rho}\right)$$

$$C_V \frac{dT}{T} = \frac{R}{\mu}\frac{d\rho}{\rho}$$

we integrate to obtain

$$C_V \ln T = \frac{R}{\mu}\ln\rho + C$$

the constant of integration becomes a multiplicative coefficient when the logarithm is taken

$$T^{C_V} \propto \rho^{R/\mu}$$

substituting in Equation A.10

$$T^{C_V} \propto \rho^{C_P - C_V}$$

$$T\rho \propto \rho^{\frac{C_P - C_V}{C_V} + 1}$$

$$T\rho \propto \rho^{C_P/C_V}$$

$$T\rho \propto \rho^{\gamma}$$

using the ideal gas law again we finally obtain

$$P \propto \rho^{\gamma} \tag{A.12}$$

Thus I have shown that

$$P = (\gamma - 1)\,\rho\epsilon \propto \rho^{\gamma} \quad .$$

for adiabatic fluids.

Appendix B

Sedov-Taylor Solution

This appendix derives, in detail, the Sedov-Taylor solution. Section B.1 derives the scaling relationship $R_s = \zeta \left(\frac{Et^2}{\rho_0}\right)^{1/5}$. Section B.2 shows how the scaling relationship can reduce the spherically symmetric Euler equations into a system of ordinary differential equations (ODEs) and section B.3 discusses the value of the scaling coefficient ζ.

B.1 Scaling Relation

As stated in Chapter 3 the Sedov-Taylor solution involves only four variables: E, the energy of the explosion; ρ_0, the ambient density; R_s, the radius of the shock wave; t, the time elapsed since the explosion. Thus

$$R_s \propto E^{\alpha} \rho_0^{\beta} t^{\gamma} \tag{B.1}$$

where α, β, and γ are exponents to be determined. If we look at the dimensionality of these variables it is clear that α, β and γ can each only take one value. First note that the units

of energy and density are

$$[E] = [M][L]^2[t]^{-2}, \quad [\rho_0] = [M][L]^{-3}$$

Combining these with relation (3.1), we get

$$[R_s] = [L] = [M]^{\alpha+\beta}[L]^{2\alpha-3\beta}[t]^{\gamma-2\alpha}$$

Giving us a system of three equations:

$$\alpha + \beta = 0, \;\; 2\alpha - 3\beta = 1, \;\; \gamma - 2\alpha = 0$$

Solving this yields

$$\alpha = 1/5, \;\; \beta = -1/5, \;\; \gamma = 2/5$$

Resulting in the Sedov-Taylor scaling relationship:

$$R_s = \zeta \left(\frac{Et^2}{\rho_0} \right)^{1/5} \tag{B.2}$$

B.2 Reducing the Euler Equations into a System of Ordinary Differential Equations

In Chapter 3 I stated that the Sedov-Taylor Scaling relation can be used to reduce the Euler equations to a system of ODEs; In this section I show this in detail. First we

define a unitless radius x as follows:

$$x \equiv \frac{r}{R_s} = \frac{1}{\zeta}\left(\frac{\rho_0}{E}\right)^{1/5} r t^{2/5}. \tag{B.3}$$

Note that both x and R_s are dependent on time. We can scale density (ρ), velocity (v) and pressure (P) in a similar manner:

$$\rho(x) = \rho_0 f(x) \tag{B.4a}$$

$$v(x) = \frac{R_s}{t} g(x) \tag{B.4b}$$

$$P(x) = \rho_0 \left(\frac{R_s}{t}\right)^2 h(x) \tag{B.4c}$$

From here on out I will not be writing out terms as explicit functions, i.e. f will be written in place of $f(x)$.

We then substitute these relations into the spherically symmetric adiabatic Euler equations:

$$\frac{\partial \rho}{\partial t} + \frac{1}{r^2}\frac{\partial}{\partial r}\left(r^2 \rho v\right) = 0 \qquad \text{(mass conservation)} \tag{B.5}$$

$$\rho\left(\frac{\partial}{\partial t} + v\frac{\partial}{\partial r}\right) v + \frac{\partial P}{\partial r} = 0 \qquad \text{(momentum conservation)} \tag{B.6}$$

$$\left(\frac{\partial}{\partial t} + v\frac{\partial}{\partial r}\right)\frac{P}{\rho^\gamma} = 0, \qquad \text{(adiabatic energy conservation)} \tag{B.7}$$

however, we need to compute some derivatives before we can work out the substitution. Note that for a generic function, $F(r,t)$, if $F(r,t) \propto t^\eta$ then

$$\frac{\partial F(r,t)}{\partial t} = \eta \frac{F(r,t)}{t}. \tag{B.8}$$

This helps us obtain the following derivatives:

$$\frac{\partial x}{\partial r} = \frac{1}{R_s} \qquad \frac{\partial x}{\partial t} = -\frac{2}{5}\frac{x}{t} \tag{B.9}$$

$$\frac{\partial \rho}{\partial r} = \frac{\rho_0}{R_s} f' \qquad \frac{\partial \rho}{\partial t} = -\frac{2}{5}\frac{x}{t}\rho_0 f' \tag{B.10}$$

$$\frac{\partial v}{\partial r} = \frac{g'}{t} \qquad \frac{\partial v}{\partial t} = -\frac{3}{5}\frac{R_s}{t^2} g - \frac{2}{5}\frac{x R_s}{t^2} g' \tag{B.11}$$

$$\frac{\partial P}{\partial r} = \rho_0 \frac{R_s}{t^2} h' \qquad \frac{\partial P}{\partial t} = -\frac{6}{5}\rho_0 \frac{R_s^2}{t^3} h - \frac{2}{5}\rho_0 \frac{x R_s^2}{t^3} h' \tag{B.12}$$

Now lets work with Equation B.5. First we need to compute $\frac{\partial}{\partial r}\left(r^2 \rho v\right)$:

$$\frac{\partial}{\partial r}\left(r^2 \rho v\right) = 2r\rho v + r^2\left(v\frac{\partial \rho}{\partial r} + \rho \frac{\partial v}{\partial r}\right)$$

Using B.10(Left) and B.11(Left)

$$= 2r\rho v + r^2\left(\frac{v\rho_0 f'}{R_s} + \rho\frac{g'}{t}\right) \tag{B.13}$$

$$= 2r\rho_0 \frac{R_s}{t} fg + r^2\left(\frac{\rho_0}{t} f'g + \frac{\rho_0}{t} fg'\right)$$

$$= 2r^2 \frac{\rho_0}{xt} fg + r^2 \frac{\rho_0}{t}\left(f'g + fg'\right) \tag{B.14}$$

Thus

$$\frac{\partial \rho}{\partial t} + \frac{1}{r^2}\frac{\partial}{\partial r}\left(r^2 \rho v\right) = -\frac{2}{5}\frac{x}{t}\rho_0 f' + 2\frac{\rho_0}{xt} fg + \frac{\rho_0}{t}\left(f'g + fg'\right) = 0$$

multiplying by $\frac{5t}{\rho_0} x$ gets us the first of our three ordinary differential equations:

$$\boxed{10fg + 5x\left(f'g + fg'\right) - 2x^2 f' = 0} \tag{B.15}$$

Fortunately we do not need to take any new derivatives to manipulate Equation B.6. By

utilizing Equations B.11(Both Sides) and B.12(Right) we get

$$\begin{aligned}\rho\left(\frac{\partial}{\partial t}+v\frac{\partial}{\partial r}\right)v+\frac{\partial P}{\partial r} &= \rho\left(-\frac{3}{5}\frac{R_s}{t^2}g-\frac{2}{5}\frac{xR_s}{t^2}g'+v\frac{g'}{t}\right)+\rho_0\frac{R_s}{t^2}h' \\ &= \rho_0 f\left(-\frac{3}{5}\frac{R_s}{t^2}g-\frac{2}{5}\frac{xR_s}{t^2}g'+\frac{R_s}{t^2}gg'\right)+\rho_0\frac{R_s}{t^2}h' \\ &= \rho_0\frac{R_s}{t^2}f\left(-\frac{3}{5}g-\frac{2}{5}xg'+gg'\right)+\rho_0\frac{R_s}{t^2}h'=0\end{aligned}$$

we then multiply by $\dfrac{5t^2}{\rho_0 R_s}$ to get our second equation:

$$\boxed{f\left(-3g-2xg'+5gg'\right)+5h'=0} \tag{B.16}$$

For the last of the Euler equations (B.7) we need to compute to more derivatives. Using Equations B.10(Left) and B.12(Left) we obtain

$$\begin{aligned}\frac{\partial}{\partial r}\frac{P}{\rho^\gamma} &= \rho^{-\gamma}\frac{\partial P}{\partial r}-\gamma\rho^{-\gamma-1}P\frac{\partial\rho}{\partial r} \\ &= (\rho_0 f)^{-\gamma}\rho_0\frac{R_s}{t^2}h'-\gamma(\rho_0 f)^{-\gamma-1}\rho_0\left(\frac{R_s}{t}\right)^2 h\frac{\rho_0}{R_s}f' \\ &= \rho_0^{1-\gamma}f^{-\gamma-1}\frac{R_s}{t^2}\left(fh'-\gamma f'h\right)\end{aligned} \tag{B.17}$$

and using Equations B.10(Right) and B.12(Right) gives us

$$\begin{aligned}\frac{\partial}{\partial t}\frac{P}{\rho^\gamma} &= \rho^{-\gamma}\frac{\partial P}{\partial t}-\gamma\rho^{-\gamma-1}P\frac{\partial\rho}{\partial t} \\ &= (\rho_0 f)^{-\gamma}\left(-\frac{6}{5}\rho_0\frac{R_s^2}{t^3}h-\frac{2}{5}\rho_0\frac{xR_s^2}{t^3}h'\right)+\gamma\rho^{-\gamma-1}\rho_0\left(\frac{R_s}{t}\right)^2 h\frac{2}{5}\frac{x}{t}\rho_0 f' \\ &= -\rho_0^{1-\gamma}f^{-\gamma-1}\left(\frac{6}{5}\frac{R_s^2}{t^3}fh+\frac{2}{5}\frac{xR_s^2}{t^3}fh'-\gamma\frac{2}{5}\frac{R_s^2}{t^3}xf'h\right) \\ &= -\rho_0^{1-\gamma}f^{-\gamma-1}\frac{R_s^2}{5t^3}\left(6fh+2xfh'-2\gamma xf'h\right)\end{aligned} \tag{B.18}$$

Using these we can now reduce Equation B.7:

$$\begin{aligned}
\left(\frac{\partial}{\partial t}+v\frac{\partial}{\partial r}\right)\frac{P}{\rho^{\gamma}} &= -\rho_0^{1-\gamma}f^{-\gamma-1}\frac{R_s^2}{5t^3}\left(6fh+2xfh'-2\gamma xf'h\right)+v\rho_0^{1-\gamma}f^{-\gamma-1}\frac{R_s}{t^2}\left(fh'-\gamma f'h\right)\\
&= -\rho_0^{1-\gamma}f^{-\gamma-1}\frac{R_s^2}{5t^3}\left(6fh+2xfh'-2\gamma xf'h\right)+\frac{R_s}{t}g\rho_0^{1-\gamma}f^{-\gamma-1}\frac{R_s}{t^2}\left(fh'-\gamma f'h\right)\\
&= \rho_0^{1-\gamma}f^{-\gamma-1}\frac{R_s^2}{5t^3}\left[-6fh-2xfh'-2\gamma xf'h+5g\left(fh'-\gamma f'h\right)\right]\\
&= \rho_0^{1-\gamma}f^{-\gamma-1}\frac{R_s^2}{5t^3}\left[(5g-2x)\left(fh'-\gamma f'h\right)-6fh\right]=0
\end{aligned}$$

Dividing by $\rho_0^{1-\gamma}f^{-\gamma-1}\frac{5R_s^2}{t^3}$ results in our final differential equation:

$$\boxed{(5g-2x)\left(fh'-\gamma f'h\right)-6fh=0} \tag{B.19}$$

B.2.1 Boundary Conditions

While we now have a system of three ordinary differential equations and the functions to solve for, boundary conditions are still needed. To derive these boundary conditions we first note that in the reference frame of the shock, the system is in a steady state. This allows us to use the one dimensional Euler equations for a steady flow (i.e. all the time

derivatives are zero).

$$\frac{d}{dx}\left(\rho v\right) = 0 \tag{B.20a}$$

$$\frac{d}{dx}\left(\rho v^2 + P\right) = 0 \tag{B.20b}$$

$$\frac{d}{dx}\left[\left(E + \frac{P}{\rho}\right)\rho v\right] = \frac{d}{dx}\left[\left(\epsilon + \frac{1}{2}v^2 + \frac{P}{\rho}\right)\rho v\right] = 0 \tag{B.20c}$$

By integrating these equations over the infinitesimal width of the shock we get the Rankine-Hugoniot equations which relate the density, velocity and pressure just in front of the shock (ρ_1, v_1, and P_1 respectively) to the same parameters just behind the shock (ρ_2, v_2, and P_2), see Figure B.1 for an illustration. The Rankine-Hugoniot equations are as follows

$$a \equiv \rho_1 v_1 = \rho_2 v_2 \tag{B.21a}$$

$$b \equiv \rho_1 v_1^2 + P_1 = \rho_2 v_2^2 + P_2 \tag{B.21b}$$

$$c \equiv \epsilon_1 + \frac{1}{2}v_1^2 + \frac{P_1}{\rho_1} = \epsilon_2 + \frac{1}{2}v_2^2 + \frac{P_2}{\rho_2}, \tag{B.21c}$$

where a, b, c are constants defined to make calculations easier. Note to obtain Equation B.21c one must utilize Equation B.21a.

From the equation of state (Equation 2.5) we get

$$\epsilon = \frac{1}{\gamma - 1}\frac{P}{\gamma}. \tag{B.22}$$

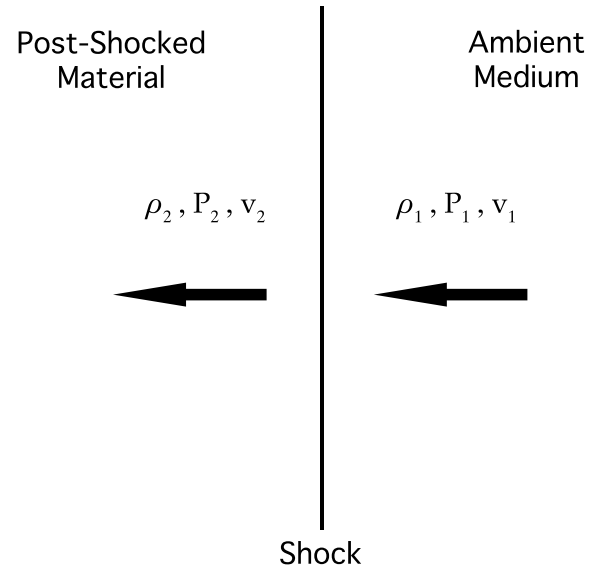

Figure B.1 Illustration of a shock in its rest frame. In this frame of reference, material in the ambient medium (shown on the right of the shock) is moving toward the shock with velocity v_1 and has density and pressure ρ_1 and P_1, respectively. This material leaves the shock to the left with velocity v_2 and has density and pressure ρ_2 and P_2 respectively.

Thus Equation B.21c yields

$$c = \frac{1}{2}v^2 + \frac{\gamma}{\gamma - 1}\frac{P}{\rho}. \tag{B.23}$$

The subscripts have been removed because this equation is valid on both sides of the shock.

At this point it is useful to find an expression for P in terms of v and the constants a and b.

$$\frac{b}{va} = 1 + \frac{P}{\rho v^2} \quad \Rightarrow \quad \frac{P}{\rho} = \frac{vb}{a} - v^2 \tag{B.24}$$

By combining this with the previous equation we get

$$c = \frac{1}{2}v^2 + \frac{\gamma}{\gamma - 1}\left(\frac{vb}{a} - v^2\right), \tag{B.25}$$

which can be written as a second degree polynomial in terms of v:

$$\begin{aligned}\left(\frac{1}{2}-\frac{\gamma}{\gamma-1}\right)v^2+\frac{\gamma}{\gamma-1}\frac{b}{a}v-c&=0\\ -\frac{\gamma+1}{2\left(\gamma+1\right)}v^2+\frac{\gamma}{\gamma-1}\frac{b}{a}v-c&=0\\ v^2-\frac{2\gamma}{\gamma+1}\frac{b}{a}v+\frac{2\left(\gamma-1\right)}{\gamma+1}c&=0,\end{aligned}\tag{B.26}$$

resulting in

$$v=\frac{\gamma}{\gamma+1}\frac{b}{a}\pm\frac{1}{2}\sqrt{\dots}\tag{B.27}$$

The value inside the radical is not important because it is more enlightening to look at the combination of the roots:

$$\begin{aligned}v_1+v_2&=\frac{2\gamma}{\gamma+1}\frac{b}{a}\\ \frac{v_2}{v_1}&=\frac{2\gamma}{\gamma+1}\frac{b}{v_1 a}-1\end{aligned}\tag{B.28}$$

note that the two roots correspond the velocity on either side of the shock. We can now simplify this expression by assuming that v_1 is much greater then the sound speed of the of the fluid (c_s),

$$v_1 \gg c_s \text{ or } \mathcal{M}_1 \gg 1,\tag{B.29}$$

where $\mathcal{M}$ is the Mach number and is defined as v/c_s. This assumption is known as the strong shock condition and in order to use this condition we must write b/a in terms of c_s, where

$$c_s^2=\gamma\frac{P}{\rho}\tag{B.30}$$

for an adiabatic fluid. This is a valid assumption because, in a shock, pressure differences are moving to fast to be equalized. Thus preventing cooling and allowing the shock to behave adiabatically. Thus using equation B.24 gives

$$\begin{aligned} \frac{c_s^2}{\gamma} &= \frac{vb}{a} - v^2 \\ \frac{1}{\gamma \mathcal{M}^2} &= \frac{b}{va} - 1 \\ \frac{b}{va} &= \frac{1}{\gamma \mathcal{M}^2} + 1. \end{aligned} \tag{B.31}$$

Using the information in Equation B.28, and noting that $b/v_1 a \approx 1$ for $\mathcal{M}_1 \gg 1$

$$\frac{v_2}{v_1} = \frac{2\gamma}{\gamma+1}\left(\frac{1}{\gamma \mathcal{M}_1^2} + 1\right) - 1 \approx \frac{\gamma - 1}{\gamma + 1},$$

reducing Equation B.21a to

$$\frac{\rho_2}{\rho_1} = \frac{\gamma+1}{\gamma-1}. \tag{B.32}$$

Now to determine the pressure we manipulate Equation B.31

$$b = v_1 a \left(\frac{1}{\gamma \mathcal{M}_1^2} + 1\right) \approx v_1 a = \rho_1 v_1^2. \tag{B.33}$$

This tells us quantitatively that the ambient pressure ($P1$) is negligible, which makes sense on a qualitative level because explosions have extremely high pressures and velocities. By utilizing this information and the definition of b (Equation B.21b) we get

$$\rho_2 v_2^2 + P_2 = \rho_1 v_1^2, \tag{B.34}$$

subtracting $\rho_2 v_2^2$ from both sides we acquire

$$\begin{aligned} P_2 &= \rho_1 v_1^2 - \rho_2 v_2^2 \\ &= \rho_1 v_1 \left(v_1 - v_2\right) \\ &= \rho_1 v_1^2 \left(1 - \frac{\gamma - 1}{\gamma + 1}\right) \\ &= \frac{2}{\gamma + 1} \rho_1 v_1^2 \end{aligned}$$

By noting that v_1 is the velocity of the shock (V_s)and that ρ_1 is the ambient density (ρ_0) we obtain

$$v_2 = \frac{\gamma - 1}{\gamma + 1} V_s \tag{B.35a}$$

$$\rho_2 = \frac{\gamma + 1}{\gamma - 1} \rho_0 \tag{B.35b}$$

$$P_2 = \frac{2}{\gamma + 1} \rho_0 V_s^2 \tag{B.35c}$$

For the Sedov-Taylor solution

$$V_s = \frac{\partial R_s}{\partial t} = \frac{2}{5} \frac{R_s}{t}. \tag{B.36}$$

Thus

$$\rho\left(1\right) = \rho_0 f\left(1\right) = \rho_2 = \frac{\gamma + 1}{\gamma - 1} \rho_0 \tag{B.37a}$$

$$v\left(1\right) = \frac{R_s}{t} g\left(1\right) = v_2 = \frac{2}{\gamma + 1} V_s \tag{B.37b}$$

$$P\left(1\right) = \rho_0 \left(\frac{R_s}{t}\right)^2 h\left(1\right) = P_2 = \frac{2}{\gamma + 1} \rho_0 V_s^2 \tag{B.37c}$$

where ρ_s and P_s are the density and the pressure of the of the shock front respectively and v_s is the velocity just behind the shock front. By solving for $f(1)$, $g(1)$ and $h(1)$ we obtain our boundary conditions and close our system of ordinary differential equations:

$$10fg + 5x\left(f'g + fg'\right) - 2x^2 f' = 0 \tag{B.38a}$$

$$f\left(-3g - 2xg' + 5gg'\right) + 5h' = 0 \tag{B.38b}$$

$$(5g - 2x)\left(fh' - \gamma f'h\right) - 6fh = 0 \tag{B.38c}$$

with boundary conditions

$$f(1) = \frac{\gamma + 1}{\gamma - 1} \tag{B.38d}$$

$$g(1) = \frac{2}{5}\frac{2}{\gamma + 1} \tag{B.38e}$$

$$h(1) = \frac{4}{25}\frac{2}{\gamma + 1} \tag{B.38f}$$

It is common to see these functions normalized to their values at $x = 1$ when plotted, so I define the normalized functions as follows:

$$\tilde{f}(x) \equiv \frac{f(x)}{f(1)} = \frac{\gamma - 1}{\gamma + 1} f(x) \tag{B.39}$$

$$\tilde{g}(x) \equiv \frac{g(x)}{g(1)} = \frac{5}{4}(\gamma + 1)\, g(x) \tag{B.40}$$

$$\tilde{h}(x) \equiv \frac{h(x)}{h(1)} = \frac{25}{8}(\gamma + 1)\, h(x) \tag{B.41}$$

These functions are plotted for $\gamma = 5/3$ in Figure B.2.

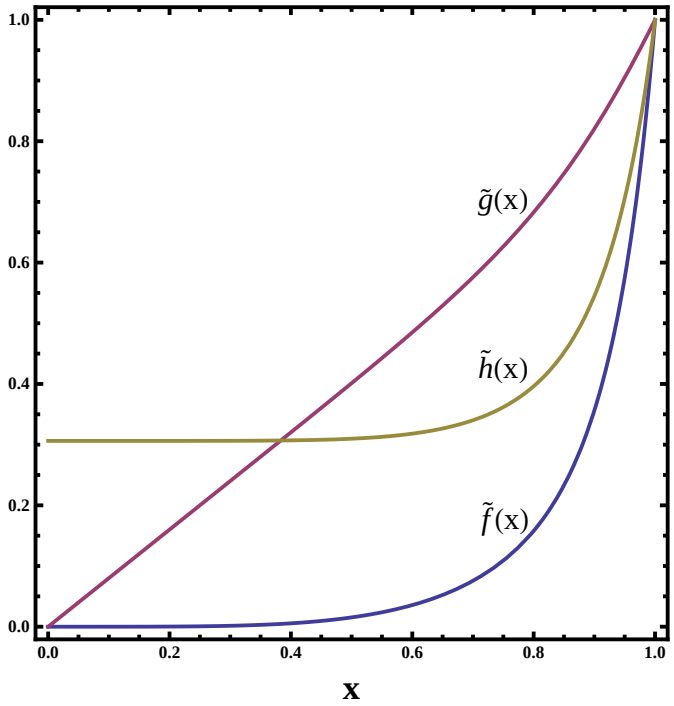

Figure B.2 Plot of the Sedov-Taylor Solution. Density (blue curve denoted by $\tilde{f}(x)$), velocity (purple curve denoted by $\tilde{g}(x)$) and pressure (gold curve denoted by $\tilde{h}(x)$) are normalized to their values just behind the shock $(x-1)$ and plotted.

B.3 Scaling Coefficient

The scaling coefficient ζ is of order unity and can be derived by examining the total energy of the system (E) which is the sum of kinetic energy and internal energy (the integration of Equation 2.4 over the mass of the system):

$$E = \int_V \rho \left(\frac{1}{2} v^2 + \epsilon \right) dV \tag{B.42}$$

We then use the equation of state (Equation 2.5) to replace ϵ (the internal energy per unit mass)

$$\epsilon = \frac{P}{\rho \left(\gamma - 1 \right)}, \tag{B.43}$$

allowing us to write the energy in terms of previously determined functions:

$$\begin{aligned} E &= \int_V \rho \left(\frac{1}{2} v^2 + \frac{P}{\rho \left(\gamma - 1 \right)} \right) dV \\ &= 4\pi \int_0^{R_s} \left(\frac{1}{2} \rho v^2 + \frac{P}{\gamma - 1} \right) r^2 \, dr \\ &= 4\pi R_s^3 \int_0^1 \left(\frac{1}{2} \rho v^2 + \frac{P}{\gamma - 1} \right) x^2 \, dx \\ &= 4\pi R_s^5 \frac{\rho_0}{t^2} \int_0^1 \left(\frac{1}{2} f g^2 + \frac{h}{\gamma - 1} \right) x^2 \, dx \end{aligned}$$

using the scaling relationship (B.2) we can introduce ζ

$$\begin{aligned} &= 4\pi \zeta^5 \frac{E t^2}{\rho_0} \frac{\rho_0}{t^2} \int_0^1 \left(\frac{1}{2} f g^2 + \frac{h}{\gamma - 1} \right) x^2 \, dx \\ &= 4\pi \zeta^5 E \int_0^1 \left(\frac{1}{2} f g^2 + \frac{h}{\gamma - 1} \right) x^2 \, dx \end{aligned}$$

Therefore

$$\zeta = \left[4\pi \int_0^1 \left(\frac{1}{2} f\left(x\right) g^2\left(x\right) + \frac{h\left(x\right)}{\gamma - 1} \right) x^2 \, dx \right]^{-1/5} \tag{B.44}$$

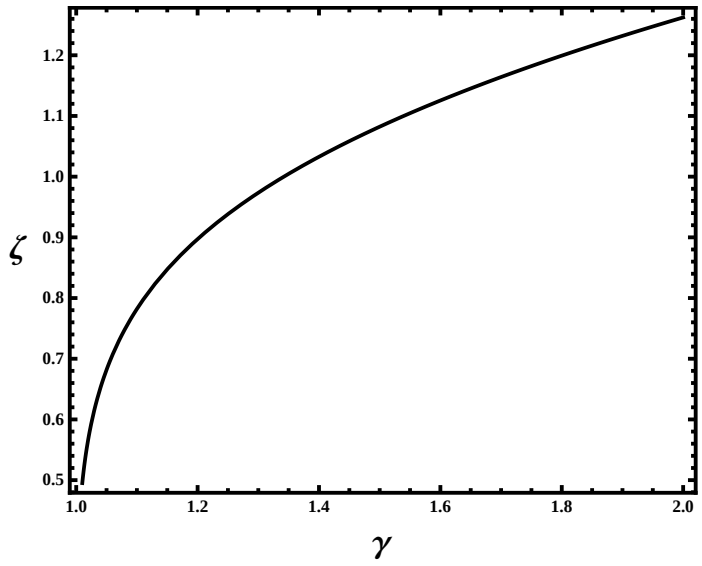

Figure B.3 Plot of the Sedov-Taylor scaling coefficient ζ verses γ. Note that ζ asymptotically approaches zero as $\gamma \to 1$.

Because $f(x)$, $g(x)$ and $h(x)$ are determined by the system of ordinary differential equations B.38a-c, ζ depend on γ in non-trivial ways (see Figure B.3). For the typical value $\gamma = 5/3$, $\zeta = 1.152$ (determined by numerical integration).

Appendix C

Simulated Stellar Group Parameters

This appendix contains the configurations of the 3D stellar groups simulated in this thesis.

Table C.1. Cantó Cluster

$x_\star$ (cm)	$x_\star$ (cm)	$x_\star$ (cm)	$\dot{M}_w$ ($M_\odot$ yr^{-1})	v_w (km s^{-1})
1.585×10^{18}	7.378×10^{17}	5.509×10^{17}	3.33×10^{-5}	600
7.446×10^{17}	-9.537×10^{17}	-5.048×10^{17}	3.33×10^{-5}	600
5.897×10^{17}	-2.005×10^{17}	-1.829×10^{18}	3.33×10^{-5}	600
-4.632×10^{16}	1.310×10^{17}	3.296×10^{17}	3.33×10^{-5}	600
-1.211×10^{18}	-3.450×10^{17}	-1.325×10^{18}	3.33×10^{-5}	600
1.318×10^{18}	-1.832×10^{17}	8.471×10^{17}	3.33×10^{-5}	600
-1.549×10^{18}	7.078×10^{17}	-9.145×10^{16}	3.33×10^{-5}	600
4.590×10^{16}	1.360×10^{17}	-1.823×10^{18}	3.33×10^{-5}	600
-6.354×10^{16}	5.678×10^{17}	-3.586×10^{17}	3.33×10^{-5}	600
-2.346×10^{17}	-8.699×10^{17}	2.029×10^{17}	3.33×10^{-5}	600

Table C.2. Vrba Group

$x_\star$ (cm)	$x_\star$ (cm)	$x_\star$ (cm)	$\dot{M}_w$ ($M_\odot$ yr^{-1})	v_w (km s^{-1})
-8.377×10^{17}	4.101×10^{17}	-2.659×10^{12}	5×10^{-6}	2000
-2.513×10^{18}	-6.109×10^{16}	3.934×10^{17}	5×10^{-6}	2000
-2.618×10^{17}	-1.789×10^{18}	-1.090×10^{18}	5×10^{-6}	2000
5.760×10^{17}	5.149×10^{17}	-9.412×10^{17}	1×10^{-4}	15
1.257×10^{18}	7.243×10^{17}	-2.205×10^{16}	1×10^{-4}	15
1.780×10^{18}	2.007×10^{17}	5.609×10^{17}	2×10^{-6}	3000
2.609×10^{17}	3.620×10^{17}	-3.218×10^{17}	2×10^{-6}	3000
5.521×10^{17}	2.096×10^{17}	6.538×10^{17}	2×10^{-6}	3000
0	0	0	1×10^{-4}	15

Appendix D

Abbreviation Used

AMR	Adaptive Mesh Refinement
AXP	Anomalous X-ray Pulsar
SGR	Soft Gamma Repeaters
BSG	Blue Supergiant
CCSN	Core Collapse Supernova
ISM	Interstellar Medium
MHD	Magnetohydrodynamics
OED	Ordinary Differential Equation
PPM	Piecewise Parabolic Method
RSG	Red Supergiant
SN	Supernova
SNR	Supernova Remnant
WR	Wolf-Rayet (Star)

Bibliography

Athanassiadou, T. 2009, PhD thesis, University of Illinois at Urbana-Champaign

Bailin, J., & Harris, W. E. 2009, ApJ, 695, 1082

Begelman, M., & Rees, M. 2010, Gravity's Fatal Attraction: Black Holes in the Universe, 2nd edn. (Cambridge University Press)

Bonnell, I. A., Bate, M. R., & Zinnecker, H. 1998, MNRAS, 298, 93

Braun, R., Goss, W. M., & Lyne, A. G. 1989, ApJ, 340, 355

Cantó, J., Raga, A. C., & Rodríguez, L. F. 2000, ApJ, 536, 896

Davies, B., Figer, D. F., Kudritzki, R., Trombley, C., Kouveliotou, C., & Wachter, S. 2009, ApJ, 707, 844

Decressin, T., Baumgardt, H., Charbonnel, C., & Kroupa, P. 2010, AAP, 516, A73+

Fields, B. D., Athanassiadou, T., & Johnson, S. R. 2008, ApJ, 678, 549

FLASH. 2009, FLASH User's Guide: Version 3.2, ASC FLASH Center, University of Chicago

Fryxell, B., et al. 2000, ApJS, 131, 273

Fryxell, B. A., M uller, E., & Arnett, D. 1989, MPI Astrophys. Rep., 449

Hillenbrand, L. A. 1997, AJ, 113, 1733

Laney, C. B. 1998, Computational Gasdynamics (Cambridge University Press)

Löhner, R. 1987, Computer Methods in Applied Mechanics and Engineering, 61, 323

Marsden, D., Lingenfelter, R. E., Rothschild, R. E., & Higdon, J. C. 2001, ApJ, 550, 397

McKee, C. F. 1974, ApJ, 188, 335

Pan, K., Ricker, P. M., & Taam, R. E. 2010, ApJ, 715, 78

Repolust, T., Puls, J., & Herrero, A. 2004, AAP, 415, 349

Rockefeller, G., Fryer, C. L., Baganoff, F. K., & Melia, F. 2005, ApJL, 635, L141

Sedov, L. I. 1946, Journal of Applied Mathematics and Mechanics, 10, 241

—. 1959, Similarity and Dimensional Methods in Mechanics (New York: Academic Press)

Taylor, G. 1950, Royal Society of London Proceedings Series A, 201, 159

van Loon, J. T., Cioni, M., Zijlstra, A. A., & Loup, C. 2005, AAP, 438, 273

Vrba, F. J., Henden, A. A., Luginbuhl, C. B., Guetter, H. H., Hartmann, D. H., & Klose, S. 2000, ApJL, 533, L17

Woods, P. M., & Thompson, C. 2006, Soft gamma repeaters and anomalous X-ray pulsars: magnetar candidates, ed. Lewin, W. H. G. & van der Klis, M., 547–586

Woosley, S. E. 1988, ApJ, 330, 218